OUKA
Osaka University Knowledge Archive

Title	Internal spatial organization of receptive fields of complex cells in the early visual cortex
Author(s)	佐々木, 耕太
Citation	大阪大学, 2007, 博士論文
Version Type	VoR
URL	https://hdl.handle.net/11094/2834
rights	
Note	

Osaka University Knowledge Archive : OUKA

https://ir.library.osaka-u.ac.jp/

Osaka University

Internal spatial organization of receptive fields of complex cells in the early visual cortex

初期視覚野複雑型細胞の空間的内部構造

A dissertation submitted to

THE GRADUATE SCHOOL OF ENGINEERING SCIENCE

OSAKA UNIVERSITY

in partial fulfillment of the requirements for the degree of

DOCTOR OF PHILOSOPHY

BY

KOTA SASAKI

佐々木　耕太

JULY 2007

Abstract

The receptive fields of complex cells in the early visual cortex are economically modeled by combining outputs of a quadrature pair of linear filters. For actual complex cells, such a minimal model may be insufficient, since many more simple cells are thought to make up a complex cell receptive field. To examine the minimalist model, I analyzed spatial relationships between the internal structure (subunits) and the overall receptive fields of individual complex cells by a two-stimulus interaction technique. The receptive fields of complex cells are more circular and only slightly larger than their subunits in size. In addition, complex cell subunits occupy similar spatial extents to simple cell receptive fields. Therefore, in these respects, the minimalist schema is a fair approximation to actual complex cells. However, there are violations against the minimal model. Simple cell receptive fields have significantly fewer subregions than complex cell subunits. And simple cell receptive fields are elongated more horizontally than vertically in general. This bias is absent in complex cell subunits and receptive fields. Thus, simple cells cannot be equated to individual complex cell subunits, and spatial pooling of simple cells may occur anisotropically to comprise a complex cell subunit. Moreover, when linear filters for complex cell subunits are examined separately for bright and dark responses, there are significant imbalances and position-displacements between them. This suggests that actual complex cell receptive fields are constructed by a richer combination of linear filters than proposed by the minimalist model.

Chapter 1. Introduction

Vision is a crucial sense for survival in mammals such as carnivores and primates. It is not only a necessity but also a luxury; we enjoy wonderful visual experiences in daily life. Amazingly, these are mental phenomena, while they are caused by physical reality. All of our percepts are attributable to the activities of myriads of neurons in the brain. First of all, how are visual signals transformed and represented in individual neurons in the brain?

Information processing in the visual cortex begins with cells known as simple cells, and their outputs are considered to be passed onto complex cells. Intensive endeavors have been devoted to elucidating how simple cells encode visual information in the receptive fields. However, this is not the case for complex cells partly due to technical difficulty. In this dissertation, I present a detailed analysis of internal spatial organization of complex cells, and compare internal structure with receptive fields to examine the possibility of spatial pooling and the hierarchical relationship between simple cells and complex cells.

1.1 Simple cell and complex cell

When Hubel and Wiesel started single unit recordings in the primary visual cortex, they first attempted to excite neurons by diffuse light and dark spot (Hubel and Wiesel, 1998). Those stimuli are effective drivers for retinal and lateral geniculate nucleus (LGN) cells (Figs. 1.1.1*A* and *B*; Kuffler, 1953), but turned out to be in vain for cortical neurons. Hubel and Wiesel recollect that the first major break was thanks to the edge of the glass slide. They discovered a neuron responding vigorously to the faint but

sharp line shadow cast on the retina by the moving edge of the glass, not by retinal stimuli they prepared. Their collaboration made a series of discoveries concerning information processing in the visual system, culminating in reception of the Nobel Prize in Physiology or Medicine in 1981.

Neurons in the primary visual cortex are driven effectively by a bar and edge stimulus having orientation optimal for them (Hubel and Wiesel, 1959). The organization of their receptive fields was examined by using a bright spot and bar stimulus, and classified into two categories (Hubel and Wiesel, 1962). If neurons satisfied the following four criteria, they were termed as simple (1) the receptive fields were subdivided into distinct ON and OFF subregions; (2) there was summation within the separate ON and OFF subregions; (3) there was antagonism between ON and OFF subregions; and (4) it was possible to predict responses to stationary and moving spots of various shapes from a map of the ON and OFF subregions (Fig. 1.1.1*C*-*G*). Otherwise, neurons were grouped as complex. They responded in a complex manner that bore little obvious relationship to the receptive fields.

Therefore, simple cells and complex cells differ substantially in a manner how they summate the distributions of light intensities in the receptive fields. To examine spatial summation property quantitatively, stationary and drifting sinusoidal gratings should be employed in addition to bar and edge stimuli. Prior to application to cortical cells, such tests were already conducted to examine the properties of spatial summation for retinal (Enroth-Cugell and Robson, 1966) and LGN cells (Shapley and Hochstein, 1975).

1.2 Simple cell

Effective stimuli for simple cells can be predicted by the organization of their receptive fields (Hubel and Wiesel, 1959, 1962). This raised a possibility that simple cells calculate a weighted linear sum for the distributions of light intensities impinged on the receptive fields, although early studies by Hubel and Wiesel were qualitative rather than quantitative. If linearity of spatial summation holds, responses measured in the space and the frequency domains must be converted to each other *via* Fourier analysis. Movshon et al. (1978a) measured line-weighting functions (space domain) for simple cells by bar stimuli elongated along the axis of optimal orientation, and compared them with contrast-sensitivity functions (frequency domain) measured with the use of sinusoidal grating stimuli of variable spatial frequency. Close match between the two measurements indicates that majority of simple cells were described fairly well as linear spatial filters (see also Jones and Palmer, 1987).

Some simple cells exhibited a systematic shift in latencies for stationary grating stimuli having different phases (Movshon et al. 1978a). This characteristic first emerges in the cerebral cortex in cats and primates (Enroth-Cugell and Robson, 1966). This was of particular interest with regard to the neuronal mechanism for selectivity to the direction of motion because this suggests that the motion computation in the early visual cortex does not rely on ‘AND’ operation (Adelson and Bergen, 1985; Watson and Ahumada, 1983, 1985; Reichardt 1961). Now the temporal dimension must be taken into account seriously for the receptive fields of simple cells. Since a monocular image projected onto the retina can be fully specified by three dimensions (two dimensions of space x, y, and one dimension of time t), the spatiotemporal characterization of receptive field structure is a complete depiction for monocular visual information processing

performed in single neurons.

It is worth addressing an issue whether the temporal integration of visual signals is also linear or not. DeAngelis et al. (1993) followed authentic linearity tests (Enroth-Cugell and Robson, 1966; Movshon et al. 1978a), which, in their case, compared the responses in the temporal domain with those in the temporal frequency domain. The spatiotemoral receptive fields were measured for simple cells by a reverse correlation technique, which is also known as a spike-triggered averaging (STA) method (Jones and Palmer, 1987; Sutter 1975). In this technique, a simple cell was simulated with a long, pseudorandom sequence of briefly flashed small bright and dark bars over a region covering the spatial receptive field (imagine white and black 'snowflakes' presented on the display). To obtain the spatial receptive field structure with a latency of τ ms, votes were cast by all stimuli preceding spikes by τ ms for contrast polarities and locations. The temporal dimension was added by varying a parameter of τ. Subtraction of the votes to dark stimuli from those to bright stimuli produced the composite receptive field map.

The temporal frequency tuning was estimated *via* Fourier analysis by the spatiotemporal receptive fields. These predictions were compared with the temporal frequency tuning measured by using drifting sinusoidal gratings. The optimal and cut-off values of temporal frequency tuning curves were generally consistent between the actual measurements and the predictions made by the spatiotemporal receptive fields. Direction selectivity indices, however, tended to be underestimated in the linear predictions compared with the actual measurements obtained by drifting grating stimuli. This systematic discrepancy was readily reconciled by expansive nonlinearity that may reflect nonlinear contrast response (Albrecht and Geisler, 1991; Albrecht and Hamilton

1982).

1.3 Complex cell

Complex cells exhibit gross nonlinear property of summation, while simple cells show linearity of spatiotemporal summation. Complex cells exhibit elevated maintained discharge for drifting sinusoidal gratings (Movshon et al. 1978b), while simple cells show modulated responses to them (a half-wave rectified sinusoidal wave in ideal cases; Movshon et al. 1978a). This is a major difference between the two cell groups. A test by an optimal sinusoidal grating has been conventionally used to quantify the degree of linearity of spatiotemporal summation performed by neurons (Li et al. 2003; Skottun et al. 1991).

The spatial extents of complex cell receptive fields are obtained by turning on and off a single bar elongated along the axis of optimal orientation. However, this simple experiment fails to uncover a manner in which complex cells summate light intensities in the receptive fields to yield selectivities to stimulus features such as orientation, spatial frequency, and so on. The functional internal structure, called *subunit*, of complex cells can be unveiled by presenting two bars simultaneously. As inferred from selectivity for spatial frequency, the relative positions and contrast polarities (bright or dark) of two bars are critical parameters to elicit responses in complex cells. Movshon et al. (1978b) first examined two-bar interaction profiles by changing the relative position and contrast polarity of the second bar while presenting the first bar somewhere in the receptive fields. The two-bar interaction profiles obtained by this method could predict the contrast-sensitivity functions measured by grating stimuli of variable spatial frequency. Therefore, these interaction profiles represent the

spatial structure of functional units acting as spatial linear filters internal to complex cells.

In terms of nonlinear systems identification, two-bar interaction profiles obtained by Movshon et al. (1978b) are intimately related to second-order Wiener kernels (Marmarelis and Marmarelis, 1978). To account for various functional characteristics of complex cells, second-order interaction analysis was extended to the temporal domain (Emerson et al. 1987), and then along the parallel axis to optimal orientation by using two-dots, rather than two-bar, stimuli (Gaska et al. 1994; Livingstone and Conway, 2003). The interaction profiles were often obtained as a variant of STA maps, in which spike votes were given to a combination of two stimuli. The general consensus of the above studies is that selectivity to orientation, the direction of motion, spatial and temporal frequency is explained well by the second-order interaction maps for complex cells.

More sophisticated spike-triggered techniques have been developed recently to estimate stimulus patterns that is associated with change in the spike statistics of neurons by using principle component analysis and/or information theoretic approach (Pillow and Simoncelli, 2006; Prenger et al. 2004; Rust et al. 2005; Sharpee et al. 2004; Touryan et al. 2002). In these methods, dynamic dense noise stimuli are presented during the recording of a spike train, and the distribution of spike-triggered stimulus patterns is compared with that of all stimulus patterns actually presented. When a certain stimulus pattern occurs more or less frequently in spike-triggered stimuli above chance, it should be associated to the enhancement or the depression of the neuronal activity, respectively. Such a pattern is related to the profile of an excitatory or a suppressive filter. All filters may be recovered which influence the firing probabilities of

neurons. This is a great advantage over traditional STA methods, which can find only a single net excitatory filter.

1.4 Experimental paradigm

One goal of systems neuroscience is to understand neural codes. This may be addressed bi-directionally: questions in the forward direction ask how individual neurons fragment, transform, and represent sensory signals, while ones in the reverse direction ask how neuronal ensembles reconstruct sensory signals presented to an animal. Inquiries in the reverse direction are beyond the scope of this dissertation.

To characterize input-output relationships, a set of stimuli was often selected in advance and/or customized during a recording session by investigators so that the response properties of neurons of interest were measured for each of them. For instance, grating stimuli having different orientations were prepared for early visual cortical neurons to measure their orientation tuning curves. This approach is practical, but it should be pointed out that it has essential fallacies.

Basically, the above experimental design aims at searching for an optimal stimulus by making a list that maps a visual stimulus to a neuronal response for each stimulus. This method can determine *which* stimulus produced the best response among stimuli in the list. However, the result cannot predict *how strong* response would be produced for an item that was not enlisted in the list. Therefore, it does not predict *what* stimulus would produce the best response; the best stimulus in the present list may not be the best any longer when a new stimulus is added to it. In the case of the above example, measurements for optimal orientation predict nothing about tuning for other stimulus parameters such as spatial frequency and size. Thus, a primary attempt to

search for an optimal stimulus cannot be fulfilled with this method.

Moreover, vision is a multidimensional sense. Even when an artificial and simple stimulus such as a sinusoidal grating is selected, many parameters may affect the responses of visual neurons: retinal position, orientation, spatial frequency, size, etc. Therefore, an ideal approach discovers dimensions actually exciting or suppressing neurons by encompassing all dimensions that potentially influence the responses. Spike-triggered analysis by using dense noise stimuli meets this requirement. Noise stimuli have advantages over other visual stimuli in terms of generality. In other words, dense noise stimuli are broadband in the frequency domain, and can represent (or imitate) any pattern in the space domain. Physiological investigation may be conducted under minimal assumption. A practical drawback of this strategy is that dense noise stimuli cannot be very efficient drivers for visual cortical neurons, and might be totally ineffective for neurons in the higher visual cortex in primates.

1.5 Functional model

Linear filters and other functional ingredients of early visual cortical neurons can be discovered by spike-triggered techniques. How well do these components predict their responses? Modern V1 neuroscientists are serious about building a model (or a theory), and making predictions based on the model, and verifying the model (or clarifying deviations from the current model for further elaboration). I am not necessarily in tune with this fashion, but still believe that this is one rational method for checking how much one understands the behavior of single neurons in the early visual cortex.

Theoretical framework and analytical techniques, including linear filter theory

and STA approaches, contributed to the physiological elucidation of the neuronal computation performed by single neurons in the early visual cortex. Now, almost 50 years have passed since early exploration by Hubel and Wiesel, and many have been added to the inventories of the functional properties of early visual cortical neurons such as adaptation (Carandini and Ferster, 1997; Movshon and Lennie, 1979; Ohzawa et al., 1982), gain control (Carandini et al. 1997; Carandini and Heeger, 1994) and various suppressive phenomena (Benevento et al. 1972; Bredfeldt and Ringach, 2002; Ringach et al. 2002).

However, most of the response properties of early visual cortical neurons can be captured concisely in functional models known as standard liner-nonlinear models (Fig. 1.5.1). The functional models are phenomenological representations for the computation preformed by single neurons. While the functional models do not intend to resemble anatomical or biophysical substrates for the computation preformed by single neurons, one can imagine parallelism between actual biology and the model. That is, the linear component may correspond to the spatiotemporal integration of postsynaptic potentials caused by synaptic transmissions. On the other hand, the nonlinear component may correspond to transformation from the membrane potential to a firing rate. The nonlinear component may be followed by a Poisson spike generator, which converts the rate signal into spikes. Such extended models are called linear-nonlinear-Poisson models.

For a simple cell, the liner-nonlinear model can be fully identified on the basis of physiological measurements (Fig. 1.5.1*A*). The linear filter corresponds to the receptive field mapped by the STA technique (DeAngelis et al. 1993; Jones and Palmer, 1987; Sutter 1975). For the output of the filter, a negative value is not observed (thus,

half-wave rectification), and a positive value is converted expansively (typically, squaring operation). The nonlinear function from physiological data can be estimated by comparing the distribution of the filter outputs of spike-triggered stimuli to that of all stimuli (Anzai et al., 1999).

By definition, complex cells show nonlinearity of spatiotemporal summation. They are insensitive to precise positions and contrast polarities of a visual stimulus. When complex cells are completely insensitive to these stimulus features, they measure the magnitude, or energy, of local contrast without regard to the precise position or polarity of stimulus. This computation can be economically performed by two linear filters of which outputs are squared and summed (Fig. 1.5.1*B*; Adelson and Bergen, 1985; Fleet et al. 1996). Because the number of linear filters is minimized in this model, this standard energy model will be referred as the minimalist energy model in this dissertation. It should be noted that, in reality, four linear filters with half-squaring operation are required for equivalent computation to account for the fact that spike output cannot transmit a negative signal (Ohzawa et al. 1990; Pollen et al. 1989).

The minimalist energy model for the receptive fields of complex cells is rather conceptual compared with the model characterization for simple cells. This is partly due to the fact that currently available methods cannot reveal two (or more) biological linear filters for the receptive fields of compel cells. Second-order interaction analysis can find not more than one filter. Recent techniques including a spike-triggered covariance (STC) cannot meet the condition, either. Although multiple filters may be recovered by these methods, the recovered filters may not represent how light signals are actually combined because of mutual orthogonality imposed on them.

However, it is still worth reviewing investigations conducted by the STC

method. Its first application for cortical neurons aimed at isolating linear filters internal to a complex cell (Touryan et al. 2002). More than three-fourth of complex cells recorded in this study had exactly two filters, as the standard energy model proposes (Fig. 1.5.1*B*). On the other hand, Rust et al. (2005) reported that additional filters were recovered in many complex cells by collecting many spikes (minimum of 50 spikes per spatiotemporal dimension), because the number of recorded spikes can be a limiting factor to the recovery of filters. Surprisingly, full-wave rectifying filters were discovered for simple cells also. Moreover, not only excitatory but also suppressive filters were recovered, and interestingly suppressive filters usually showed opposite direction preference to excitatory ones. This indicates that neurons in the early visual cortex can perform a very intricate computation to compare the strength of visual features moving in opposite directions (Adelson and Bergen, 1985). Therefore, the richness of neuronal computation remains to be unveiled in early visual cortical neurons.

1.6 Subunit

Subunits refer to the internal functional structure revealed by second-order interaction analysis for complex cells (Livingstone and Conway, 2003; Movshon et al. 1978b; Ohzawa and Freeman, 1986; Rust et al. 2005). Subunits are spatial (or spatiotemporal) linear filters themselves, and resemble linear filters in the energy model closely (Figs. 1.5.1*B* and *C*). However, subunits should be contributed by multiple underlying linear filters in the neuronal circuitry in the brain. In this sense, subunits are different from linear filters in the energy model, because linear filters in the energy model do not have underlying component filters. Moreover, plausible contribution from

many filters suggests that subunits are virtual entities and do not represent single anatomically identifiable cells.

1.7 Hierarchical model

The nervous system is organized in a hierarchical fashion. Therefore, it is natural to consider that the receptive field of a cortical simple cell is constructed by afferent inputs from LGN neurons (Fig. 1.7.1*A*; Hubel and Wisel, 1962). More specifically, Hubel and Wiesel (1962) proposed that an ON subregion in the receptive field of a simple cell is generated by a group of ON-center LGN cells that are aligned specifically in the simple cell ON subregion, while an OFF subregion is generated by OFF-center LGN cells in such a manner. To examine this model, receptive field maps were obtained simultaneously from cortical simple cells and LGN neurons, and rules to govern their connectivity were investigated (Reid and Alonso, 1995; Alonso et al. 2001). Between a monosynaptically connected pair of cells, the center of an LGN receptive field tended to overlap a subregion with matched sign (ON or OFF) in a simple cell receptive field. Moreover, opposite-sign overlap was rarely observed between such a pair. This is consistent with the hierarchical model between cortical simple cells and LGN cells (Hubel and Wiesel, 1962).

The hierarchical model was extended to a relationship between cortical cells. Hubel and Wiesel (1962) suggested that a complex cell is constructed by collecting inputs from simple cells for which receptive fields all have identical axis orientation, but differ from one another in their exact retinal positions (Fig. 1.7.1*B*). This hypothesis is consisted of three parts. (1) A complex cell is constructed by collecting inputs from simple cells. (2) The receptive fields of simple cells all have identical axis orientation

(identical orientation). (3) But they differ from one another in their exact retinal positions (spatial pooling). These three components will be treated as separate hypotheses for clarity in this dissertation. The identical orientation hypothesis appears obvious, because haphazard convergence from cells that prefer various orientation results in the deterioration of orientation tuning (see also Alonzo and Martinez, 1999). In the remaining of this dissertation, the hierarchical model refers to the first part, which proposes that a complex cell is constructed by collecting inputs from simple cells, because a word 'hierarchy' is derived from a possible hierarchical relationship between simple cells and complex cells. The possibility of spatial pooling is not considered in this nomenclature.

Physiological evidence for the hierarchical model is scarce and rather controversial. A pioneer cross-correlation study by Toyama et al. (1981) investigated functional connectivity between many pairs of intracortical neurons, and found no excitatory connections from a simple cell to a complex cell. On the other hand, such connections were reported from a simple cell in layer IV to a complex cell in layer II/III (Alonso and Martinez, 1999; Martinez and Alonso, 2001). Direct and strong evidence for the hierarchical model should discuss the filter structure internal to a complex cell in terms of the organization of an antecedent simple cell receptive field. Unfortunately, the above studies examined the overall spatial extent of complex cell receptive fields, instead of internal functional filters of complex cells.

Recent theoretical (Chance et al. 1999; Mechler and Ringach, 2002) and experimental (Priebe et al. 2004) investigations have questioned the rigid hierarchical organization between simple cells and complex cells. As a matter of fact, both cell groups may be generated in an 'egalitarian' network (Tao et al. 2004). The hierarchical

relationship between simple cells and complex cells have been commonly believed partially by the fact that the degree of modulated spike responses to optimal drifting sinusoidal gratings shows a bimodal distribution for a population of early visual cortical neurons (Li et al. 2003; Skottun et al. 1991). This bimodality, however, does not necessarily imply two distinct classes of neurons, because the bimodal distribution may be generated from a unimordal distribution by a nonlinear transformation rule which converts membrane potentials into spike rates (Mechler and Ringach, 2002). When it is measured based on membrane potentials instead of spike rates, the degree of the modulation to optimal drifting sinusoidal gratings became a continuous distribution (Priebe et al. 2004). Moreover, simple cells and complex cells form almost identical distributions in this measure.

1.8 Spatial pooling

The spatial extents in which two visual stimuli can interact are limited to those of biological substrates of linear filters. Therefore, the hierarchical model predicts that the spatial properties of subunits, which are obtained by second-order interaction analysis, resemble those of simple cell receptive fields closely. The minimalist energy model has the smallest number of linear filters to achieve insensitivity to precise positions and contrast polarities of visual stimuli, and the linear filters are located at identical positions and occupy spatial extents between themselves (Fig. 1.5.1*B*; Adelson and Bergen, 1985; Fleet et al. 1996). This proposes that the size of the subunit is identical to that of a complex cell receptive field.

However, if simple cells are pooled extensively in space in order to generate a complex cell (Fig. 1.5.1*C*), the spatial extents of the subunit must be limited to a small

portion of the receptive field of a complex cell. The possible extensive spatial pooling of simple cells to comprise a complex cell is inferred by at least three pieces of evidence. (1) A hand-plotting mapping study for receptive fields reported that the receptive field sizes of complex cells were on average three times larger than those of simple cells (Hubel and Wisel, 1962). (2) The binocular interaction profiles of complex cells tend to be elongated more than those of simple cells (Sanada and Ohzawa, 2005). Spatial pooling of simple cells may explain the elongation of the binocular interaction profiles for complex cells. (3) Connection between a pair of neurons is so weak that simultaneous contributions from many cells are required to excite a postsynaptic cell (~10% correlation strength on average for a pair of cells with identical orientation preference (difference <22°); Alonso and Martinez, 1999).

The spatial properties of subunits will be characterized with the use of second-order interaction analysis, and related to those of the receptive fields for individual complex cells. What is the shape of the subunits and the overall receptive fields of complex cells? Are subunits pooled spatially to comprise the receptive field of a complex cell? Is the composition of linear filters consistent with that proposed by the energy model? In addition, comparisons of properties of these subunits with those of simple cell receptive fields are also presented in order to examine the details of the hierarchical model of complex cell receptive fields.

Chapter 2. Materials and Methods

I recorded single units in area 17 of 37 adult cats. All animal care and experimental guidelines conformed to those established by the National Institute of Health (Bethesda, MD) and were approved by the Osaka University Animal Care and Use Committee.

2.1 Surgical procedure and animal maintenance

After initial preanesthetic doses of hydroxyzine (Atarax, 2.5 mg im) and atropine (0.05 mg im), each cat was anesthetized with isoflurane (2-3.5% in O_2) for the remainder of the surgical preparation. Lidocaine was injected subcutaneously or applied topically at all points of pressure and possible sources of pain. Electrocardiogram (ECG) electrodes were secured, a rectal temperature probe was inserted, and a femoral vein was catheterized. Body temperature was maintained near 38°C with the use of a feedback-controlled heating pad for the remainder of the experiment. Subsequently, a tracheostomy was performed, and a glass tracheal tube was inserted for artificial respiration. The animal was then secured in a stereotaxic apparatus with the use of ear and mouth bars and clamps on the orbital rim. Anesthesia was then switched to sodium thiopental (Ravonal, 1.0 $mg \cdot kg^{-1} \cdot h^{-1}$ iv). After the stabilization of anesthesia, the animal was paralyzed with a loading dose of gallamine triethiodide (Flaxedil, 10 $mg \cdot kg^{-1} \cdot h^{-1}$ iv) to minimize eye movements during single unit recording, and placed under artificial ventilation with a gas mixture of 70% N_2O-30% O_2. End-tidal CO_2 was maintained at a constant level of 3.5-4.3% throughout the experiment. For the remainder of the experiment, the infusion fluid was delivered, containing sodium thiopental (Ravonal,

1.0 $mg \cdot kg^{-1} \cdot h^{-1}$ iv), gallamine triethiodide (Flaxedil, 10 $mg \cdot kg^{-1} \cdot h^{-1}$ iv), and glucose (40 $mg \cdot kg^{-1} \cdot h^{-1}$ iv) in lactated Ringer solution. In addition to body temperature and end-tidal CO_2, heart rate, ECG, and intratracheal pressure were monitored and maintained within a normal range throughout the experiment. Pupils were dilated with atropine (1%), and nictitating membranes were retracted with phenylephrine hydrochloride (Neosynesin, 5%). Contact lenses with 4-mm artificial pupils were then placed on each cornea.

A craniotomy was carried out above the central representation of the visual field in visual area 17 approximately at the Horseley-Clarke coordinate, P4-L2.5. This corresponds to < 10 degrees in retinal eccentricity. The dura was removed to permit the insertion of tungsten microelectrodes for single unit recording. Setting the electrodes close to the cortical surface, agar was applied over the cortex for protection, and melted wax was applied over the agar to create a sealed chamber for stabilization. When the electrodes were retracted, electrolytic lesions (5 μA, 5 s) were made at 700-1,500 μm intervals for each electrode track. Typically, recordings from an animal lasted four days.

At the end of an experiment, the animal was administered an overdose of pentobarbital sodium (Nembutal), and perfused through the heart with formalin (4% in buffered saline). The recorded areas were frozen, sectioned into 40-60 μm slices, and stained with thionin. The locations of electrode tracks were identified.

2.2 Single unit recording

Lacquer-coated tungsten microelectrodes (1-5 MΩ; A-M Systems, Sequim, WA) were used to record single unit activities. Typically, two electrodes mounted in a single protective guide tube were driven in parallel with a common microelectrode drive to increase the chance of encountering neurons. The signals from the electrodes were

amplified (10,000×), bandpass filtered (300-5,000 Hz), and fed into a custom-made data acquisition computer system (Ohzawa et al. 1996). The data acquisition system consisted of analog-to-digital converters and a spike waveform discriminator that sorted signals from each electrode in real time. The time-stamped spike events (time resolution, 40 μs) were sent from the data acquisition system, along with their waveforms, to a separate computer that controlled the experiment. This second computer saved to files the spike data and other events, including the onset and the offset times of each trial and stimulus presentations, parameters and conditions of the spike sorter, and the entire set of experimental parameters. The stored data were analyzed on a third computer during and after the experiment.

2.3 Visual stimulation

Generations of visual stimuli were performed using custom-built software on yet another computer. At the request of the experiment control computer noted above, visual stimuli were generated by the fourth computer controlling a graphics card (Millenium G550; Matrox, Dorval, Quebec, Canada), and displayed on a cathode ray tube monitor (76Hz frame rate, 1600 × 1024 pixels; GDM-FW900; Sony, Tokyo, Japan) through the green channel only to avoid color misconvergence across channels. In each experiment, the luminance nonlinearity of the display was measured using a photometer (Minolta CS-100; Konica Minolta, Osaka, Japan), and linearized by gamma-corrected lookup tables. The animal saw the display through a custom-built haploscope, which allows visual stimuli to be presented to the left and right eyes separately (Sanada and Ohzawa, 2006). A black separator was placed between the left and right visual fields to preclude the projection of stimuli to unintended eyes. Distance (total length of light

paths) between the screen and the eyes was set to 57 cm, subtending the visual field of 23° × 30° for each eye.

2.4 Recording procedure

When a single unit was isolated, preliminary observations were made to determine its optimal orientation, spatial frequency, as well as the position and the size of its receptive field. In this "search" procedure, the orientation, spatial frequency, position, and size of a patch of drifting sinusoidal grating could be adjusted with the use of a pointing device (mouse). Having completed the above procedure, tuning in the orientation and spatial frequency domain was measured for the cell by presenting flashed sinusoidal grating stimuli (Nishimoto et al. 2005) and/or drifting sinusoidal grating stimuli. The degree of response modulation was assessed by presenting sinusoidal grating with a combination of orientation and spatial frequency that elicited the largest number of spikes. The cell was then classified into simple or complex on the basis of the amplitude of the first harmonic component relative to the average firing rate (F_1/F_0 ratio; Li et al. 2003; Skottun et al. 1991).

To evaluate the receptive field structure, I presented dynamic two-dimensional noise stimuli with 51 × 51 small dots. The noise stimuli covered an area typically two to three times larger than the receptive field of the neuron in both the horizontal and the vertical directions. Each dot was assigned with dark (~3 cd·m^{-2}), bright (~90 cd·m^{-2}), or gray luminance (~47 cd·m^{-2}) at equal probability. The gray dots had the same luminance value as the mean luminance of the display. The dot size was determined for each cell primarily based on optimal spatial frequency to achieve both sufficient spatial resolution and signal-to-noise ratio (0.12° × 0.12° to 0.67° × 0.67° for individual dots; 5.3 dots per

subregion width on average). The noise pattern was refreshed at every 26 or 13 ms, which corresponded to two or one video frame, respectively. The presentation of the dynamic noise stimuli lasted about 30 min for collecting a sufficient number of spikes for the following data analysis.

2.5 First-order map and second-order interaction map

Monocular visual stimuli, S, can be fully characterized by two dimensions of space (x, y) and one of time (t), $S(x, y, t)$. The two-dimensional dynamic noise stimuli used in this study consisted of three luminance values, 0, -1, 1, which corresponded to gray, dark, bright dots, respectively. Spike-triggered stimuli were of particular interest among $S(x, y, t)$.

For simple cells, the first-order maps were calculated to analyze the receptive field structure.

The first-order map, $h_1(x, y, \tau)$, represents the linear component of neuronal responses, and was obtained by the spike-triggered averaging of $S(x, y, t_i - \tau)$

$$h_1(x,y,\tau)=\sum_{i=1}^{N} S(x,y,t_i - \tau)$$

where N is the total number of spikes collected during the stimulus presentation, and i is an index for the i-th spike, which was produced at time t_i. The first-order map was obtained for correlation delays ranging from 0 to 289 ms in 13 ms (one video frame duration) intervals.

For complex cells, the second-order interaction maps were computed to examine the internal structure of their receptive fields. This procedure is schematically illustrated in Fig. 2.5.1.

The second-order interaction map, $h_2(x_1, x_2, y_1, y_2, \tau_1, \tau_2)$, was calculated by

accumulating the product of two spike-triggered stimuli, namely $S(x_1, y_1, t_i - \tau_1)$ and $S(x_2, y_2, t_i - \tau_2)$ for the i-th spike

$$h_2(x_1,x_2,y_1,y_2,\tau_1,\tau_2) = \sum_{i=1}^{N} S(x_1,y_1,t_i-\tau_1)\cdot S(x_2,y_2,t_i-\tau_2)$$

$$= \sum_{i=1}^{N} S(x_1,y_1,t_i-\tau_1)\cdot S(x_1+dx,y_1+dy,t_i-\tau_1-d\tau)$$

where dx and dy represent spatial displacements between the two stimuli, and $d\tau$ corresponds to a temporal offset between them. Thus, the second-order interactions are described by the six-dimensional function.

This computation casts a positive vote for an interaction between the stimuli with the same contrast polarity (dark-dark and bright-bright), and a negative vote for an interaction between those with the opposite contrast polarity (dark-bright, bright-dark). When at least one member of a pair of stimuli is a gray dot, no vote is presented. This calculation is, therefore, essentially identical to one used for sparse noise stimuli in previous studies (Gaska et al. 1994; Livingstone and Conway, 2003).

To obtain a second-order interaction map, one stimulus location was selected as the reference and fixed at a particular spatial coordinate (x_1, y_1) and a particular correlation delay τ_1 as shown in Fig. 2.5.1*B*. Then, the second-order interaction map for the reference (x_1, y_1, τ_1) was calculated within the local neighborhood of this reference, as indicated by the dashed square in Fig. 2.5.1*B*. The spatial displacements for dx and dy ranged from -10 to 10 stimulus dots. Empirically, this extent for the second-order analysis was sufficiently wide for containing significant interactions. The second-order interaction with itself (i.e. $dx = 0$, $dy = 0$, and $d\tau = 0$) cannot be measured with ternary dense noise stimuli, since overlapping stimuli cannot be represented. For further analysis, the value at zero displacement was filled in by a spline interpolation from

neighboring pixels in the interaction map. Since the two-stimulus interaction profiles are strongest and occupy the largest spatial extent between simultaneously presented stimuli in general (Anzai et al. 2001; Gaska et al. 1994), the temporal offset $d\tau$ was always set to 0 ms to evaluate the spatial structure and extent of second-order interaction maps. Accumulation of votes for all spikes produced the second-order interaction map for the reference (x_1, y_1, τ_1). By changing the values of x_1, y_1, and τ_1, second-order interaction maps were obtained for references at every dot locations in visual stimuli for correlation delays from 0 to 197 ms in 13 ms (one video frame duration) steps.

2.6 Second-order interaction map and subunit

The term *subunit* has been used extensively for referring to a functional or virtual unit that operates as a linear spatial (or spatiotemporal) filter internal to a complex cell (Livingstone and Conway, 2003; Movshon et al. 1978b; Ohzawa and Freeman, 1986; Rust et al. 2005). In this report, I define a subunit as a functional unit that is described by a second-order interaction profile as explained above. A subunit is closely related to, but is not identical to linear filters depicted in models for complex cells (Figs. 1.5.1*B* and *C*). As mentioned in the previous reports, a subunit contains contributions from multiple linear filters, presumably simple cells according to the hierarchical model (Hubel and Wiesel, 1962), and therefore does not represent a single anatomically identifiable cell.

2.7 Data analysis

First-order receptive fields and subunits in second-order maps are usually

modulated along an axis perpendicular to the optimal orientation. I obtained their spatial extents by using a partial Hilbert transform (Hahn, 1992). This method for obtaining an envelope is applicable for any multi-dimensional data modulated along a single axis, because it does not assume a specific functional form. Alternatively, my maps could have been fitted by a model function selected *a prioi,* and its envelopes may have been extracted for subsequent analyses. A reasonable candidate for such a model function is a Gabor function, as employed by most recent studies dealing with simple cell receptive fields. However, some second-order maps of complex cells may have broader flanking subregions than a central one (Szulborski and Palmer, 1989). This characteristic is not captured well by a Gabor function, thus I avoided fitting second-order maps by it.

Here, the partial Hilbert transform was carried out in the two-dimensional spatial frequency domain along an axis perpendicular to the optimal orientation. First, the two-dimensional Fourier transform of the map was computed. Then, the spatial frequency domain was divided into two mirror symmetrical halves about the axis perpendicular to a vector pointing to the optimal orientation and spatial frequency from the origin. As a result, each half of the spatial frequency domain had spectral components that are identical in amplitude and are different in the sign of imaginary parts. The spatial frequency components in one half were shifted by 90° in phase. For the other half, they were shifted by -90° in phase. The inverse Fourier transform of the result yielded a complex signal where the real parts retained the original signal (Fig. 2.5.1*E*) and formed a quadrature pair with the imaginary parts (Fig. 2.5.1*F*). The envelope of the map (Fig. 2.5.1*G*) was obtained by calculating the absolute value (amplitude) of the complex signal. Since the second-order interaction maps were obtained for all dot locations in visual stimuli, some of maps were outside the complex

cell receptive field and contained no signal. For these maps, the axis for the partial Hilbert transform could not be determined. Likewise, for cells without significant orientation tuning or spatial antagonism, the axis could not be determined either. Therefore, for these cases, the absolute values of interaction maps themselves were used as their envelopes.

In previous studies, the second-order interaction maps were often averaged across all reference positions within the receptive field of a complex cell to enhance signal-to-noise ratios for a single final map (Emerson et al. 1987; Gaska et al. 1994; Livingstone and Conway, 2003). This means that the six dimensional interaction maps, $h_2(x_1, x_1+dx, y_1, y_1+dy, \tau_1, \tau_1+\mathrm{d}\tau)$, were reduced to just three dimensions of dx, dy, and $d\tau$. In this approach, the original maps were assumed to be spatially homogeneous. This assumption is justified for some complex cells (Emerson et al. 1987), but not for others (Szulborski and Palmer, 1990). Therefore, I have examined second-order interaction maps and their envelopes for all individual reference positions separately. I assume that the strength of a second-order subunit is proportional to the collective responses of underlying linear filters contributing to that subunit. With this assumption, the overall receptive field of a complex cell may be obtained by collecting the envelopes of the second-order interaction maps. A complex cell receptive field at a correlation delay of τ was obtained as follows. First, I squared the envelopes of second-order interaction maps at a delay τ at all reference locations. The squaring operation was incorporated to approximate the effects of power-law static nonlinearities at the outputs of subunits (Gaska et al. 1994). Then, the squared envelopes were summed into a larger map (Fig. 2.5.1*H*) at their respective positions. Finally, its square root was computed. For further analysis, an optimal correlation delay was determined at which the amplitude of the

receptive field was at maximum. I found that >95% interaction maps exhibited the strongest interactions at the optimal correlation delay. This supports that the receptive field size was estimated appropriately because of constancy in timing across interaction maps.

As describe above, the receptive field envelopes of a simple cell were obtained in 13-ms intervals. These were then spline-interpolated along the time axis in 1-ms steps. For a correlation delay where the interpolated envelope had the maximum response, the receptive field and its envelope were computed for further analysis.

I evaluated the spatial shape for the second-order interaction envelopes and the receptive fields of complex cells, and the receptive field envelopes of simple cells. To extract parameters for characterizing them, each of them was fitted by a two-dimensional Gaussian function having the form

$$G(x,y)=B+K\exp\left(-\frac{x'^2}{2\sigma_{x'}^{\ 2}}-\frac{y'^2}{2\sigma_{y'}^{\ 2}}\right)$$
$$x'=(x-x_0)\sin\theta-(y-y_0)\cos\theta$$
$$y'=(x-x_0)\cos\theta+(y-y_0)\sin\theta$$

where B, K, x_0, y_0, $\sigma_{x'}$, $\sigma_{y'}$, and θ are free parameters. Specifically, the spatial coordinate (x_0, y_0) corresponds to the center position, and θ rotates the translated coordinate system to align x and y axes with the major and minor axes of the Gaussian function. $\sigma_{x'}$ and $\sigma_{y'}$ are measures of the spatial extent. B is a baseline parameter, and K is simply a scaling factor. The Gaussian fit accounted for 70% of variance in data on average.

Spatial properties for the subunits and receptive fields were quantified on the basis of the parameters of the best fitted Gaussian function. To evaluate size parameters such as length, width, and area, a bound was drawn at a criterion level that is 5% of the peak amplitude of the fitted Gaussian function. For this boundary, length and width

were measured along the parallel and perpendicular axes to the optimal orientation, respectively. Fig. 2.7.1 schematically shows the length and the width for the subunits and the receptive fields of complex cells. The length and the width for the receptive fields of complex cells were defined with respect to the optimal orientation of the subunits with the highest amplitude. For the receptive fields of simple cells, the length and the width were obtained for the optimal orientation. Optimal orientation was obtained via Fourier analysis, and is a parameter independent of the major axis of the fitted Gaussian function.

Chapter 3. Results

I analyzed data from 86 complex cells in area 17 of adult cats. Of these, three neurons were recorded in penetrations in the area 17/18 border zones, but their tuning properties such as the receptive field size and optimal spatial frequency were close to those of average area-17 cells. Therefore, these cells are included in the rest of the analyses. To compare spatial properties between complex cell subunits and simple cell receptive fields, I also analyzed data from 152 simple cells in area 17. Simple and complex cells were classified based on the ratio of the first harmonic amplitude to the mean discharge rate for responses to drifting sinusoidal gratings (Li et al. 2003; Skottun et al. 1991). For complex cells, the spatial structure of subunits and receptive fields were computed through the second-order interaction analysis. As described in the previous section, second-order interaction maps were calculated at a temporal offset = 0 between the reference and neighboring stimuli, i.e., between two simultaneously presented stimuli. To obtain second-order interaction maps with sufficient signal-to-noise ratios, the analysis requires more spikes than the first-order analysis. Thus, our sample contained fewer complex cells than simple cells, for which receptive fields were calculated through the first-order analysis. The average numbers of spikes collected during one measurement with the dynamic noise stimuli were 9867.7 ± 9221.8 for complex cells and 4454.2 ± 3935.0 for simple cells (mean ± SD). The minimum numbers of spikes were 649 and 180 for complex and simple cells, respectively. Likewise, the maxima were 47115 and 20017.

One of the major purposes of this study is to examine spatial pooling of subunits that collectively comprise the receptive fields of single complex cells. To achieve this goal, spatial characteristics are compared between the subunits and the

overall receptive fields for individual complex cells. If the hierarchical model of Hubel and Wiesel (1962) is correct (Alonso and Martinez, 1998; Martinez and Alonso, 2001; but see also Toyama et al. 1981), subunits of a complex cell should closely reflect properties of simple cells contributing inputs to it. Although simple cells in my population were recorded separately from complex cells and do not have direct connection to the complex cells, I am able to compare the two cell types as groups. Specifically, it is worth comparing corresponding parameters between the subunits of complex cells and the receptive fields of simple cells. The simple and complex cells were recorded from the same set of electrode tracks in the same animals using 2-d dynamic noise stimuli, although the proportions of cell types varied from one track to another.

3.1 Second-order interaction maps

Fig. 3.1.1 shows a representative example of the second-order interaction analysis for a complex cell. In *A*, interaction maps are tiled to reflect the spatial locations of their references. Although the references may be at every dot location of the stimuli, the results are displayed here for reference positions at every two stimulus dots. The interaction maps at the top-left and center in *A* are partially overlapping in the actual stimulus domain as indicated on a noise stimulus frame (Fig. 3.1.1*B*), and outlined by dashed and thick lines, respectively. The interaction maps vary in shape depending on reference positions (Szulborski and Palmer, 1990). The central interaction map in *A* is also shown magnified in panel *C*. To determine the spatial extent of a subunit in the map, the partial Hilbert transform (Hahn, 1992) was performed as shown in *D*, and then the envelope was obtained as shown in *E*. Note that *C* and *D* differ in

spatial phase by 90° and hence form a quadrature pair. To illustrate the bounds of the interaction map, dashed line is drawn in *C* and *E* at a criterion level that is 5% of the peak height of the two-dimensional Gaussian function fitted to the envelope of the interaction map. By taking the square root of the sum of the squared envelope maps for all reference positions, the receptive field of the complex cell was obtained as shown in *F*.

In principle, the size of the overall receptive field of a complex cell may be much larger than those of individual interaction envelopes if there is extensive spatial pooling. However, there was little spatial pooling for this cell. Therefore, the region depicted in *F* is cropped to match the spatial position and scale of *C*, *D*, and *E* for ease of comparison. The bounds for the overall receptive field were again determined using a criterion amplitude that was 5% of the peak height of the Gaussian function fitted to the receptive field. This area is marked by a solid contour in *F*, and also shown in *C* and *E* for size comparison with the size of the subunit. Note that the solid and dashed contours in *C* and *E* are nearly superimposed exactly, indicating that the subunit size was nearly the same as that of the overall receptive field for this complex cell. The reference position of the interaction map in *C* was at the center of the receptive field, and therefore showed the strongest interactions among all reference locations.

The degree of spatial pooling of subunits may be quantified by the difference in spatial extent between the subunits and the overall receptive field. When the outputs of many subunits are pooled across different spatial positions to generate an overall receptive field, its size should occupy a much larger spatial extent than those of individual subunit envelopes. However, when pooling is absent, the size of a receptive field is expected to be identical to those of subunit envelopes. Therefore, the complex

cell depicted in Fig. 3.1.1 exhibited hardly any spatial pooling. The absence of spatial pooling is in fact what is predicted by the minimalist energy model. Therefore, the energy model is an accurate representation of the cell in Fig. 3.1.1.

Fig. 3.1.2 shows data from another complex cell in the same format as that for Fig. 3.1.1. For this cell, the size of the overall receptive field (solid ellipse in Fig. 3.1.2*C*, *E*, and *F*) was significantly larger than that of the subunit envelope (dashed ellipse; 169% in terms of area; $P < 0.05$, resampling). Therefore, spatial pooling of subunits did take place for this neuron.

Are there complex cells with concentric second-order interaction maps showing poor orientation selectivity (Szulborski and Palmer, 1990)? Among 86 complex cells, I found only one neuron that exhibited such characteristics as shown in Fig. 3.1.3. The subunits were round, and appeared to have a weak antagonistic surround (Fig. 3.1.3*C*). However, due to its weak contribution, the subunit envelope was essentially determined by the central region alone (Fig. 3.1.3*D*). Since the optimal axis of the partial Hilbert transform could not be determined for this neuron, the envelopes of the interaction maps were obtained by taking the absolute values of them. The size of the receptive field (solid ellipse in Fig. 3.1.3*C*, *D*, and *E*) is much larger than that of the subunit envelope (dashed ellipse; 473% in terms of area; $P < 0.05$, resampling). This complex cell showed the largest degree of spatial pooling in my sample.

For five other complex cells, Fig. 3.1.4 shows the second-order interaction maps, their envelopes, and the overall receptive fields. For each example in this figure, the interaction map illustrated was obtained with the reference position at the center of the Gaussian function fitted to the receptive field of the cell. Using the same criteria as used in Figs. 3.1.1-3, solid and dashed contours are drawn to demarcate the bounds of

receptive fields and second-order interactions, respectively. Fig. 3.1.4*C* illustrates a cell that had the largest number of subregions within a subunit among all the complex cells I analyzed. Fig. 3.1.4*D* depicts a complex cell that exhibited a substantial spatial pooling of subunits along the axis of the optimal orientation, but not along the width dimension.

For the vast majority of complex cells, the neuronal activities were recorded with dynamic noise stimulation to their dominant eye alone. However, responses to dynamic noise stimuli were measured for both eyes separately in a few binocular neurons. Figs. 3.1.4*E* and *F* show results for the second-order interaction analysis for a single complex cell in the right and the left eyes, respectively. Interaction maps as well as the receptive field profiles were highly similar for the two eyes.

3.2 Length and width

Having examined interaction maps and the extent of pooling for representative complex cells, I now analyze these properties for the population of cells I have recorded. In the population analyses, complex cell subunits were sampled at the center of the receptive fields. First, what relationships are found between the length and the width for complex cell subunits, receptive fields, and simple cell receptive fields? Fig. 3.2.1*A* shows a relationship between the length and the width for the subunits of complex cells. The length and the width were defined with respect to the optimal orientation (obtained via Fourier analysis) for the subunits (Fig. 2.7.1). To make a cell-by-cell comparison of the two values possible, subunit length is plotted against subunit width. Each circle in the scatter plot represents a datum from one complex cell. Note that the majority (63%) of circles lie above the identity line. The histograms show the distributions of the length

(right) and the width (upper) for subunits, with median values of 4.05° and 3.63°, respectively, as indicated by arrows. The subunit length was generally longer than the subunit width (P = 0.0042, Wilcoxon sign rank test).

Are complex cell receptive fields circular in shape or are they elongated along a specific direction? Fig. 3.2.1*B* shows a relationship between the length and the width for the receptive fields of complex cells. Again, the length and the width of receptive fields were measured with respect to the optimal orientation of their subunits (Fig. 2.7.1). On average, the receptive fields of complex cells were longer along the length axis than the width axis (P = 0.015, Wilcoxon sign rank test). However, the degree of elongation was not as significant as that for subunits. The median values of the receptive field length and the width were 4.72° and 4.40° (arrows), respectively.

Fig. 3.2.1*C* illustrates a relationship between the length and the width for the receptive fields of simple cells. Each circle in the scatter plot denotes a datum from a simple cell. The histograms show the distributions of the length (right) and the width (upper) for the receptive fields of simple cells, respectively. The majority (65%) of symbols are above the identity line. The median length was 4.40°, and the median width was 4.00°. This difference was statistically significant (P < 0.001, Wilcoxon sign rank test). This was exactly the same trend as observed for the subunits of complex cells as shown in Fig. 3.2.1*A*. Are the distributions of subunit length and width similar to those of receptive fields of simple cells? The answer is yes, and there was not a significant difference in either the length or the width (P > 0.05, Mann-Whitney U test).

3.3 Number of subregions

A chief functional characteristic of the early visual cortical neurons is

selectivity for orientation and spatial frequency (Hubel and Wiesel, 1959, 1962; Movshon et al. 1978a, b). Among various mechanisms contributing to the determination of tuning parameters (Benevento et al. 1972; Bredfeldt and Ringach, 2002; Ringach et al. 2002), the number of subregions in complex cell subunits is inversely related to tuning bandwidths for orientation and spatial frequency (Gaska et al., 1994; Movshon et al. 1978b). The number of subregions for a subunit was calculated as follows

$$Number\,of\ subregions = width \times SFopt \times 2$$

where *width* is the subunit width (see Fig. 2.7.1) and *SFopt* is the optimal spatial frequency obtained from the Fourier analysis of the second-order interaction map at the center of the complex cell receptive field. The product of the subunit width and the optimal frequency gives the number of cycles within the subunit. Therefore, this value is doubled to convert it into number of subregions because one cycle of modulation contains two subregions. Fig. 3.3.1*A* shows the distribution of the number of subregions in the subunits of complex cells. The mean of this distribution was 3.21, and the SD was 1.08. These values are roughly comparable to those reported by Movshon et al. (1978b).

Does the number of subregions match between the subunits of complex cells and the receptive fields of simple cells? Fig. 3.3.1*B* shows the distribution of the number of subregions within the receptive fields of simple cells. The number of subregions for simple cell receptive fields was calculated in the same manner as that for complex cell subunits. The median number of subregions within the receptive fields of simple cells was 2.53, which was significantly different from 3.00, the median number of subregions within the subunits of complex cells ($P < 0.001$, Mann-Whitney U test; see also Fig. 3.3.1*A*). Therefore, the subunits of complex cells tended to have significantly more subregions than simple cells. This difference may be related to the

fact that subunits are functionally defined units and cannot be equated to individual simple cells (Movshon et al. 1978b; Rust et al. 2005).

3.4 Length-to-width ratios and aspect ratios

Fig. 3.4.1*A* compares length-to-width ratios between subunits and receptive fields. Note that length-to-width ratios are aspect ratios defined with respect to the preferred orientation. However, I reserve the term, aspect ratios, to refer only to those related to the elliptic elongation of subunit envelopes and complex cell receptive fields (see below). There was a strong correlation between the two ratios (r = 0.81). The two distributions also had indistinguishable medians (1.12 and 1.04 for the length-to-width ratios of subunits and receptive fields, respectively, as indicated by arrows; $P > 0.05$, Wilcoxon sign rank test). These results appear to indicate that shapes of subunits are reflected directly to those of the overall receptive fields of complex cells.

With respect to length-to-width ratios, do simple cell receptive fields have indistinguishable distributions from those for complex cell subunits? Fig. 3.4.1*B* shows the distribution of length-to-width ratios for the receptive fields of simple cells. The median of the distribution was 1.08. There was not a significant difference in the median values of length-to-width ratios between the receptive fields of simple cells (Fig. 3.4.1*B*) and the subunits of complex cells (Fig. 2.10*A* top; $P > 0.05$, Mann-Whitney U test).

The direction of receptive field elongation, if any, can be different and may be independent of the preferred orientation of a neuron in general (Fig. 2.7.1). A similar distinction also applies for properties of subunits. Are complex cell receptive fields more elongated in a particular direction than their subunits? Is there any relationship

between the direction and degree of subunit elongation and pooling? To address these questions, I quantified the degree of elongation by aspect ratios, which were defined by the length ratios of major and minor axes for subunit envelopes or complex cell receptive fields.

Fig. 3.4.2*A* compares aspect ratios between the subunit envelopes and the receptive fields of complex cells. The two ratios were correlated ($r = 0.68$). The median value of the distribution of aspect ratios for receptive fields, 1.28, was significantly smaller than that for subunits, 1.32 ($P < 0.001$, Wilcoxon sign rank test). This indicates that the receptive fields of complex cells are more circular in shape than the subunits. The reduction of aspect ratios may be caused by the spatial pooling of subunits, which will be examined in the section below entitled as *Pooling of subunits*.

Fig. 3.4.2*B* shows the distribution of aspect ratios for the receptive fields of simple cells. The median of the distribution was 1.34, which was not significantly different from that for the subunits of complex cells, 1.32 ($P > 0.05$, Mann-Whitney U test; see also the upper histogram in Fig. 3.4.2*A*). Therefore, both the length-to-width ratios and the aspect ratios were consistent between the receptive fields of simple and the subunits of complex cells, as a population.

3.5 Orientation of elongation

There may be a bias in the elongation of the subunit envelopes and the receptive fields of complex cells with respect to the absolute horizontal and vertical. Scatter plots in Fig. 3.5.1 show aspect ratios against the orientation of the major axis for subunit envelopes (left) and receptive fields (right). These two quantities show no systematic relationship for respective panels. The horizontal solid line is drawn at an

arbitrary criterion level (aspect ratio = 1.2) to determine whether subunit envelopes and receptive fields are sufficiently elliptic for the subsequent analysis. For subunit envelopes and receptive fields with small aspect ratios (≤ 1.2; open symbols), their major axis cannot be determined reliably. On the other hand, those with large values (> 1.2; filled symbols) were judged as sufficiently elliptic, and were counted in histograms to examine the distributions of the orientation of the major axis (n = 66 for subunit envelopes, n = 56 for receptive fields). These distributions were not different from uniform distributions ($P > 0.05$, Kolmogorov-Smirnov test). Therefore, the results show no special orientation bias in the aspect ratios for both subunits and overall receptive fields of complex cells.

The prominent ‘oblique effect’ is reported for the distribution of preferred orientations of simple cells (Li et al. 2003). Does the orientation of receptive field envelopes of simple cells exhibit any biases? Fig. 3.5.2 shows a relationship between the orientation of the major axis for the receptive field envelopes for simple cells, and their optimal orientation. These values were measured counterclockwise from the horizontal axis in visual scene (0°). Based on the same criterion as that used in Fig. 3.5.1, the receptive field envelopes were classified as elongated (aspect ratio > 1.2; filled symbols; n = 114) or circular (aspect ratio ≤ 1.2; open symbols; n = 38). Simple cells that prefer horizontal orientation (0° and 180°) appear less likely to have vertically elongated receptive field envelopes (90°). To investigate the biased elongation of receptive field envelopes regardless of optimal orientation, the number of simple cells was counted in the top histogram (for cells with sufficiently elongated envelopes). Its striking U shape demonstrates a general tendency in which there were more simple cells with horizontally elongated envelopes than those elongated vertically ($P < 0.05$,

Kolmogorov-Smirnov test for uniform distribution).

Since optimal orientation seems related to the elongation angle of receptive field envelopes for simple cells, length-to-width ratios are evaluated in terms of optimal orientation in Fig. 3.5.3*A*. Circles, triangles, and square symbols denote neurons that prefer low, middle, and high spatial frequency, respectively. Most of cells that prefer horizontal orientation (0° and 180°) appear to have length-to-width ratios above one. This means that these cells tended to be elongated along the length, or the horizontal, axis, which is consistent with the biased distribution in Fig. 3.5.2. A solid curve and error bars indicate the geometric mean and SD values of the length-to-width ratios for simple cells grouped based on the optimal orientation in 30° steps. The variances of the length-to-width ratios were significantly different across these groups ($P < 0.05$, Bartlett test). The receptive fields of simple cells pointed to by arrows in Fig. 3.5.3*A* are illustrated as representative examples in Figs. 3.5.3*C*-*J*.

Optimal spatial frequency was also related to length-to-width ratios (Fig. 3.5.3*B*). Circles, triangles, and square symbols denote simple cells that prefer horizontal, oblique, and vertical orientations, respectively. Neurons that prefer low spatial frequency tended to exhibit low length-to-width ratios, i.e. elongated along the width axis, while those that prefer high spatial frequency were elongated along the length axis in general. A positive correlation is evident between optimal spatial frequency and length-to-width ratios ($r = 0.31$). The median values of the length-to-width ratios were significantly different across different spatial frequency groups ($P < 0.01$, Kruskal-Wallis test).

3.6 Pooling of subunits

To evaluate the degree of the spatial pooling of subunits that make up complex cells, a pooling ratio in terms of area was calculated for each neuron

$$Areal\ pooling\ ratio = \frac{the\ area\ of\ the\ receptive\ field}{the\ area\ of\ the\ subunit\ envelope}$$

The areas were those enclosed within the 5% contours defined previously (see Figs. 3.1.1-4). To achieve response invariance to contrast polarity, the simplest version of the energy model for complex cells posits a minimal number of linear filters, which forms a quadrature pair, and their outputs are squared and combined. In this model, there is no spatial pooling as defined in Fig. 1.5.1*C* because the subunit size matches the receptive field size of a complex cell. Therefore, the areal pooling ratio is predicted to be close to one. On the other hand, much larger values for the areal pooling ratio are expected when subunits are pooled spatially. The histogram of Fig. 3.6.1*A* shows the distribution of the areal pooling ratios observed for 86 complex cells. The median of the areal pooling ratios was 1.21. In length or width terms, this amounts to a 10% difference on average. These values indicate that, if anything, the spatial extents of receptive fields of complex cells were only slightly larger than those of the subunits. For each complex cell, a bootstrap test was performed to assess whether the areal pooling ratio was significantly different from one. For 32 out of 86 cells (37%), the areal pooling ratio was significantly larger than one ($P < 0.05$, resampling; black bars).

Deep layers are thought to have neurons with large receptive fields (Gilbert, 1977). Thus, the laminar dependence of the areal pooling ratios was examined for complex cells having areal pooling ratios more than 1.5. Based on limited laminar analyses for tracks for which histological determinations of layers were carried out with confidence (29% of cells), cells with the large areal pooling ratios were present in both

deep layers and supra-granular layers. For example, the cell with a circular subunit profile and the largest areal pooling ratio (4.73; Fig. 3.1.3) among my sample was recorded at the cortical depth of 180μm, which must be in layer 2. This neuron was not likely to be a special complex cell, because it had a receptive field size of less than two degrees and had almost no spontaneous discharge. Therefore, unfortunately, I did not have a neuron in my sample, which was positively identified as a special complex cell (Gilbert, 1977). A complete picture on the laminar distribution of cells with large pooling ratios requires further investigation.

It is possible that my analyses might underestimate the receptive field sizes of complex cells, if weak subregions of subunits were to be missed in noisy maps. This could lead to incorrect estimation of the degree of spatial pooling. If this were the case, quality of data would have influenced the number of subregions in subunits and the areal pooling ratios. Thus, a signal-to-noise ratio was calculated for each subunit. Signal can be considered as an amplitude parameter obtained by the Gaussian function fitted to the subunit envelope. Noise level was estimated as the SD of amplitudes of envelopes that were obtained by correlating spike sequence I actually recorded to stimulus noise patterns I did not present but with otherwise identical statistical properties. Examination of the signal-to-noise ratios of subunits revealed no systematic relationships with the number of subregions in subunits or the areal pooling ratios.

Figs. 3.6.1*B* and *C* compare the sizes of complex cell subunits, receptive fields, and simple cell receptive fields. By using hand-plotting mapping protocol for the minimum response fields, Hubel and Wiesel (1962) reported that the receptive fields of complex cells were, on average, three times larger than those of simple cells. The median of the receptive field areas of simple cells I recorded was 2.42 degree^2. And

those of the subunit areas and the receptive field areas of complex cells were 1.93 and 2.89 degree^2, respectively. I found that the receptive fields of simple cells have the equal spatial extents to the subunits and the receptive fields of complex cells ($P > 0.05$, Mann-Whitney U test).

Is there any particular axis along which pooling of subunits tends to occur? As shown in Fig. 3.4.2*A*, aspect ratios are smaller for the receptive fields of complex cells than for the subunits. Decrease in the aspect ratios can be readily explained, if subunits are pooled more extensively along the minor axis of their envelopes. To examine the possible radial anisotropy of spatial pooling, the degree of pooling was evaluated directionally along radial axes that were at various angles with the major axis of subunit envelope, as illustrated in Fig. 3.6.2*C*. Specifically, the sizes were measured along each radial axis for the subunit envelope and the receptive field. The directional pooling ratio was defined as the receptive field size divided by the subunit envelope size. Directions were then searched for which the directional pooling ratios are maximal and minimal.

Fig. 3.6.2*A* shows the distributions of the directional angle at which the maximal directional pooling occurs (left), and those for the minimal pooling (right). The directions for maximal and minimal pooling are not necessarily orthogonal to each other. The subunit envelopes of complex cells were grouped as sufficiently elliptic (aspect ratio > 1.2; filled symbols) or not (open symbols) in the scatter plots. Only complex cells with sufficiently elliptic subunit envelopes were accumulated in the histograms above. For neurons for which the areal pooling ratio was significantly larger than one ($P < 0.05$, resampling), the data are represented by black circles in the scatter plots and by black bars in the histograms. For cells without pooling, the data are shown by gray circles and by gray bars. Remarkably, the directional angle is clustered around 90° and

–90° for the maximal directional pooling ratios, and 0° for the minimal pooling ratios. This means that pooling tended to occur along the direction for which the subunits were skinnier. Therefore, the result is consistent with the above hypothesis for reconciling the discrepancy of aspect ratios between subunit envelopes and receptive fields. The distributions of the directional angle for both the maximal and the minimal directional pooling ratios were significantly different from a uniform distribution ($P < 0.001$, Kolmogorov-Smirnov test for uniform distribution).

Fig. 3.6.2*B* depicts the average ± SE values of the directional pooling ratios as a function of the angle from the subunit major axis. The difference in the pooling ratios across different directional angles was statistically significant ($P < 0.001$, Friedman test).

3.7 Subunit organizations of complex cells underlying contrast-sign invariance

How do complex cells acquire response invariance to the sign or polarity of contrast of visual stimuli? The minimalist scheme, often used in modeling, for response invariance to contrast polarity is a full-wave rectification of the outputs of two linear filters that differ in spatial phase by 90° (Adelson and Bergen, 1985; Fleet et al. 1996). In reality, biological substrates for the linear filters feeding into a complex cell are selective for the contrast polarity, and their outputs are half-wave rectified. Functionally, therefore, linear filters must be organized as a push-pull pair (Ohzawa et al. 1990; Pollen et al. 1989; Troyer et al. 1998). In theory, members of such push-pull pairs should have receptive fields that are inverted versions of each other, as assumed by various energy model schemes (Adelson and Bergen, 1985; Emerson et al. 1992; Ohzawa et al. 1990). However, there is no guarantee that this is actually the case for real

complex cells. Therefore, I will examine positive and negative halves of subunit organizations by sorting separately the second-order response maps according to the contrast polarity of reference stimuli (Emerson et al. 1987; Livingstone and Conway, 2003).

Together with second-order interaction maps, Fig. 3.7.1 depicts bright-minus-dark maps for dark and bright reference stimuli separately for four complex cells. These maps in a given row were obtained at the identical location at which the strongest second-order interactions were observed for each cell. The left panel shows a bright-minus-dark map when a dark stimulus was presented as the reference, and the center panel shows a bright-minus-dark map when a bright stimulus was presented as the reference. The gray scale is matched between the two maps. As described in *Materials and Methods*, the subtraction of these bright-minus-dark maps yielded a second-order interaction map as shown in the right panel. (Multiplication by a negative (dark) reference corresponds to subtraction.) The reference location is denoted by the cross hairs in each map. Different biological substrates are recruited by visual stimuli having opposite contrast polarities as the reference, and, in ideal complex cells, the two bright-minus-dark maps should be an inverted version of each other. This appears to be the case for cells illustrated in Figs. 3.7.1*A* and *B*.

However, in general, the two bright-minus-dark maps could not be related by simply inverting the sign for other complex cells. For a cell shown in Fig. 3.7.1*C*, the center positions of the envelopes are different between the bright-minus-dark maps. Although these maps cannot be equated to the receptive fields of simple cells, it is tempting to consider that these responses are contributed by separate populations of antecedent simple cells for which receptive fields are displaced along the width

direction (e.g. Rust et al. (2005)). Another cell depicted in Fig. 3.7.1*D* shows imbalance in amplitude as well as the displacement of the center positions between the two bright-minus-dark maps.

All four complex cells presented here exhibit even-symmetric second-order interaction maps (the right-most column) as reported previously (Emerson et al. 1987; Gaska et al. 1994; Livingstone and Conway, 2003). However, a distinction must be made between my second-order maps and those of previous studies. For previous results, due to simple methodological reasons, the interaction maps were guaranteed to be even-symmetric because the maps were averaged for all reference positions. Since each of my maps is for a single reference position, there is no such methodological basis for the symmetry. Therefore, the even symmetry in my maps represents the true nature of the two-stimulus interaction sampled near the center of the complex cell receptive fields. In fact, examinations of interaction maps near the fringes of complex cell receptive fields often revealed asymmetric interaction maps (see maps in the fifth row in Fig. 3.1.1*A*).

In contrast to the second-order interaction maps, however, internal organizations of subunits exhibited various response patterns to dark and bright reference stimuli. The bright-minus-dark maps can show different center positions and unequal strength between dark and bright references.

The minimalist energy model predicts that, when the reference is located at the center of a complex cell receptive field, the bright-minus-dark maps for dark and bright references have (1) centers at the reference location and (2) identical amplitude. These predictions are obviously violated in some complex cells as shown in Figs. 3.7.1*C* and *D*. Thus, I evaluated deviations from the model predictions for a population of complex

cells actually recorded. First, the envelope for a bright-minus-dark map was computed by partial Hilbert transform. Then, a Gaussian function was fitted to the envelope, and the parameters for center position and amplitude were examined. The center position was measured from the reference location and converted into spatial phase angle with respect to the optimal spatial frequency when the center was projected onto the width axis (the axis orthogonal to the optimal orientation for the subunit).

Fig. 3.7.2 illustrates the distributions of center position and amplitude for the envelopes of bright-minus-dark maps for dark (left) and bright (right) references. Neurons shown in Fig. 3.7.1 are indicated by the corresponding labels. The center position expressed as a phase angle represents a spatial offset, thus it was not artificially wrapped into a range from –180° to 180°. However, the actual data points were scattered within the range. The amplitude was normalized by the SD of the amplitude values on the edges of the bright-minus-dark map envelope, which is considered to represent the noise level. Therefore, the normalized amplitude may be thought of as a signal-to-noise ratio. Both of the distributions show an inverted-V shape centered about zero, indicating that maps with high amplitudes tended to have its center at the reference location. This is consistent with the minimalist energy model. However, the center position could be distant from the reference location as the amplitude decreased.

It is still possible that centers are at an identical position between the dark- and bright-reference maps if their centers are shifted in the same direction to the same amount. Fig. 3.7.3 shows the ratio of amplitudes against the difference in center positions between the two maps. For this analysis, 78 complex cells were selected for which the normalized amplitude exceeded three for both dark- and bright-reference maps. As noted above, the minimalist energy model predicts no difference in center

positions and identical amplitudes between the two maps, as marked by the cross hairs. In contrast, actual complex cells exhibited a variety of combinations between these two parameters. The two bright-minus-dark map envelopes differ in center positions by 48.2° ± 41.7° (mean ± SD). And the stronger of the bright-minus-dark maps had an amplitude 1.53 ± 1.38 times larger than that of the weaker one (mean ± SD). Therefore, although the minimalist energy model is generally capable of explaining various properties of complex cells, subunits comprising actual complex cells do not necessarily follow the "ideal" scheme, e.g., often showing amplitude differences greater than 50%.

Chapter 4. Discussion

I have studied the internal spatial organization of complex cells in the early visual cortex with the use of the second-order interaction analysis. Previous studies examined the spatiotemporal characteristics of the second-order interaction maps of complex cells in an attempt to account for selectivity to orientation, direction, and spatial and temporal frequency (Emerson et al. 1987; Gaska et al. 1994; Livingstone and Conway, 2003; Movshon et al. 1978b). Instead of focusing on tuning for these stimulus parameters, I have examined the spatial and structural relationships between the receptive field of a complex cell and their subunits as revealed through the second-order interaction maps. The results are summarized in Table 4.1.

4.1 Comparison of spatial properties between subunit envelopes and receptive fields for complex cells

A notion often held regarding complex cells is that their receptive fields tend to be large compared with simple cells, occupying an area three times as large on average (Hubel and Wiesel, 1962). A prediction based on this idea is that a large number of simple cells must be combined hierarchically for constructing a complex cell receptive field. To my surprise, this initial expectation was not fulfilled in general. When examined quantitatively, the sizes of receptive fields of complex cells on average were only slightly larger (1.21 times in area) than those of their subunit envelopes (Fig. 3.6.1*A*). The sizes of receptive fields for simple cells were also comparable to those of subunits for complex cells. Therefore, the casually held notion is not correct for typical complex cells.

What could be the sources of the discrepancy between the Hubel and Wiesel's result and mine? Sampling biases between the cell types are unlikely to be the cause because my simple and complex cells were from the same set of electrode penetrations. Although individual tracks varied in their eccentricity and ratio of cell types, these factors should not influence the overall distributions for the entire population of cells. Furthermore, I have obtained about 10 pairs of simultaneously recorded simple and complex cells. The receptive field sizes of simple and complex cells within a given pair were always closely similar. Essentially the same results, obtained for the relationships between the complex cells and their subunits, and those between the simple and complex cells, also strengthen my results.

It is possible that the "minimum response field" plotting (Bishop and Henry, 1972) used in typical hand mapping of receptive fields may miss weak subregions of simple cells, thereby underestimating the receptive field size. This problem would be more acute if only a bright bar is used in mapping (which is true for nearly all early studies including those by Hubel and Wiesel), because a dark-excitatory subregion of a simple cell may not generate any OFF response if the temporal response is monophasic (Fig. 5*B* of DeAngelis et al. 1995). In such cases, even a very strong dark-excitatory subregion would be missed, leading to an underestimation of receptive field area in excess of a factor of two or more. On the other hand, however, complex cells are not likely to be affected by this problem because, by definition, ON and OFF subregions are overlapping for these cells and the use of a bright bar only is not an obstacle for estimating the receptive field size correctly.

4.2 Spatial pooling of subunits

In theory, if there is a substantial degree of spatial pooling, the second-order interaction for a particular reference location can be limited to a portion of the receptive field, and do not necessarily cover the entire spatial extent of the receptive field of a complex cell. However, in the cat early visual cortex, I have demonstrated that subunits obtained by the second-order interaction analysis are pooled spatially only to a small degree for most cells. In other cortical areas, such a pooling does take place. For example, Pack et al. (2006) measured second-order interaction maps for MT neurons in the spatiotemporal domain, to study the direction selectivity, and found that the spatial extent of two-stimulus interaction is limited to a small portion in the receptive field. Since neurons projecting from the primary visual cortex to MT are predominantly direction-selective complex cells (Movshon and Newsome, 1996), complex cells having the receptive fields in various positions might serve as subunits that are pooled spatially to comprise the receptive field of a MT cell. Note that my results do not prove or disprove pooling of simple cells in making up spatially larger subunits. This is because summation of multiple linear receptive fields cannot be distinguished from a single large linear receptive field.

4.3 Subunit organizations of complex cells underlying contrast-sign invariance

The seminal characteristic of complex cells is that ON and OFF responses may be elicited everywhere within the receptive field (Hubel and Wiesel, 1959, 1962). Such insensitivity to the contrast polarity is thought to be achieved by combining the outputs of multiple simple cells that are sensitive to the contrast sign. Internal structures of these complex cells have been studied with various nonlinear systems analysis techniques,

most of which have assumed symmetrical structures for the contrast sign (e.g. Marmarelis and Marmarelis, 1978). However, actual complex cells do not necessarily respond identically to dark and bright stimuli (e.g., Fig. 1*B* of Ohzawa et al. 1990). Therefore, I have examined second-order interaction maps separately for the bright and dark reference stimuli. This analysis demonstrated that, contrary to the energy model assumption, the two maps could not be related to each other simply by inverting signs. The unmatched positions of bright-minus-dark maps could account for the fact that complex cell subunits have more subregions than simple cells. Together with the position-displacement, the imbalanced amplitudes between these maps might contribute to produce "imperfect" complex cells, which exhibit a minor degree of response modulation (e.g. $0.2 < F_1/F_0$ ratio < 0.8) when a drifting sinusoidal grating is presented.

4.4 Relationship to other studies on internal organizations of complex cell receptive fields

Second-order interaction maps represent how two visual stimuli interact to elicit the responses of complex cells. Thus, they may be interpreted as one possible set of linear filters for explaining complex cell responses, although they do not necessarily correspond to biological entities such as the receptive fields of simple cells that feed into complex cells.

Several spike-triggered techniques are also suited for revealing the filter structure of complex cells. Recently developed STC techniques discover multidimensional axes, or filters, relevant for explaining the variance structure of spike-triggered stimuli in the multidimensional space (Rust et al. 2005; Touryan et al. 2002). These methods rely on principal component analysis to minimize the number of

filters by imposing mutually orthogonal relationships on them. Therefore, a set of recovered filters can economically span the entire subspace in which neuronal responses are increased (excitatory filters) and decreased (suppressive filters). This has an advantage over second-order interaction analysis, which reveals only a single net excitatory filter for each reference position. However, filters recovered by the STC can be too large in spatial extent, in the sense that visual stimuli may not interact in the entire spatial extents of recovered filters to elicit neuronal responses and shape tuning for stimulus features (Rust et al. 2005). Therefore, even though neither the map obtained from the second-order interaction analysis nor that from the STC technique represents responses of a single biological entity, the second-order interaction maps are closer to the biological reality, in that they accurately reflect the spatial limits within which linear summation of stimuli takes place.

Other promising methods examine the net excitatory and inhibitory responses of complex cells in the spatial frequency domain. With these techniques, spike-triggered stimuli are first converted to their spectra in the spatial frequency domain by the Fourier transform, and then they are averaged in the frequency domain separately for different phases (David et al. 2004) or without regard to phase (Nishimoto et al. 2006; Ringach et al. 1997). Spectral representation potentially enables suppressive responses, such as suppression at low spatial frequency and cross-orientation suppression, to be dissociated from excitatory responses (Bredfeldt and Ringach, 2002; Nishimoto et al. 2006; Ringach et al. 2002). These suppressive responses are masked by excitatory responses in second-order interaction analysis, because they are usually overlapped in the space domain.

4.5 Comparison of spatial properties between complex cell subunits and simple cell receptive fields

As a population, the receptive fields of simple cells were comparable to complex cell subunits in width, length, width-to-length ratios, and aspect ratios. However, complex cell subunits contain more subregions than simple cell receptive fields. This is consistent with my findings that bright-minus-dark maps for dark and bright reference stimuli are often displaced, and therefore underlying linear filters for complex cells do not necessarily form a push-pull pair. Another interesting fact is that the receptive field envelopes of simple cells tended to be elongated horizontally rather than vertically. Complex cells, on the other hand, exhibited no such bias either for the subunits or for the receptive fields. Therefore, multiple simple cells could feed into a complex cell in an anisotropic manner such that the bias toward the horizontal elongation of their receptive fields is weakened.

In this dissertation, I have examined spatial relationships between the subunits and receptive fields for individual complex cells. My strategy is a logical practical step toward understanding how the receptive fields of complex cells are built up from simple cells, as modeled by Hubel and Wiesel (1962). In order to obtain the unequivocal answer, future studies must compare subunit properties of complex cells to those of antecedent simple cells that are directly connected to them (Alonso and Martinez, 1998).

References

Adelson EH, Bergen JR. Spatiotemporal energy models for the perception of motion. *J Opt Soc Am A* 2: 284-299, 1985.

Albrecht DG, Geisler WS. Motion selectivity and the contrast-response function of simple cells in the visual cortex. *Vis Neurosci* 7: 531-546, 1991.

Albrecht DG, Hamilton DB. Striate cortex of monkey and cat: contrast response function. *J Neurophysiol* 48: 217-237, 1982.

Alonso JM, Martinez LM. Functional connectivity between simple cells and complex cells in cat striate cortex. *Nat Neurosci* 1: 395-403, 1998.

Alonso JM, Usrey WM, Reid RC. Rules of connectivity between geniculate cells and simple cells in cat primary visual cortex. *J Neurosci* 21: 4002-4015, 2001.

Anzai A, Ohzawa I, Freeman RD. Neural mechanisms for processing binocular information I. Simple cells. *J Neurophysiol* 82: 891-908, 1999.

Anzai A, Ohzawa I, Freeman RD. Joint-encoding of motion and depth by visual cortical neurons: neural basis of the Pulfrich effect. *Nat Neurosci* 4: 513-518, 2001.

Bishop PO, Henry GH. Striate neurons: receptive field concepts. *Invest Ophthalmol* 11: 346-354, 1972.

Benevento LA, Creutzfeldt OD, Kuhnt U. Significance of intracortical inhibition in the visual cortex. *Nat New Biol* 238: 124-126, 1972.

Bredfeldt CE, Ringach DL. Dynamics of spatial frequency tuning in macaque V1. *J Neurosci* 22: 1976-1984, 2002.

Carandini M, Ferster D. A tonic hyperpolarization underlying contrast adaptation in

cat visual cortex. *Science* 276: 949-952, 1997.

Carandini M, Heeger DJ. Summation and division by neurons in primate visual cortex. *Science* 264: 1333-1336, 1994.

Carandini M, Heeger DJ, Movshon JA. Linearity and normalization in simple cells of the macaque primary visual cortex. *J Neurosci* 17: 8621-8644, 1997.

Chance FS, Nelson SB, Abbott LF. Complex cells as cortically amplified simple cells. *Nat Neurosci* 2: 277-282, 1999.

David SV, Vinje WE, Gallant JL. Natural stimulus statistics alter the receptive field structure of v1 neurons. *J Neurosci* 24: 6991-7006, 2004.

DeAngelis GC, Ohzawa I, Freeman RD. Receptive-field dynamics in the central visual pathways. *Trends Neurosci* 18: 451-458, 1995.

DeAngelis GC, Ohzawa I, Freeman RD. Spatiotemporal organization of simple-cell receptive fields in the cat's striate cortex. I. General characteristics and postnatal development. *J Neurophysiol* 69: 1091-1117, 1993.

Emerson RC, Bergen JR, Adelson EH. Directionally selective complex cells and the computation of motion energy in cat visual cortex. *Vision Res* 32: 203-218, 1992.

Emerson RC, Citron MC, Vaughn WJ, Klein SA. Nonlinear directionally selective subunits in complex cells of cat striate cortex. *J Neurophysiol* 58: 33-65, 1987.

Enroth-Cugell C, Robson JG. The contrast sensitivity of retinal ganglion cells of the cat. *J Physiol* 187: 517-552, 1966.

Fleet DJ, Wagner H, Heeger DJ. Neural encoding of binocular disparity: energy models, position shifts and phase shifts. *Vision Res* 36: 1839-1857, 1996.

Gaska JP, Jacobson LD, Chen HW, Pollen DA. Space-time spectra of complex cell filters in the macaque monkey: a comparison of results obtained with pseudowhite

noise and grating stimuli. *Vis Neurosci* 11: 805-821, 1994.

Gilbert CD. Laminar differences in receptive field properties of cells in cat primary visual cortex. *J Physiol* 268: 391-421, 1977.

Hahn SL. Multidimensional complex signals with single-orthant spectra. *Proc IEEE* 80: 1287-1300, 1992.

Hubel DH, Wiesel TN. Receptive fields of single neurones in the cat's striate cortex. *J Physiol* 148: 574-591, 1959.

Hubel DH, Wiesel TN. Receptive fields, binocular interaction and functional architecture in the cat's visual cortex. *J Physiol* 160: 106-154, 1962.

Hubel DH, Wiesel TN. Early exploration of the visual cortex. *Neuron* 20: 401-412, 1998.

Jones JP, Palmer LA. The two-dimensional spatial structure of simple receptive fields in cat striate cortex. *J Neurophysiol* 58: 1187-1211, 1987.

Kuffler SW. Discharge patterns and functional organization of mammalian retina. *J Neurophysiol* 16: 37-68, 1953.

Li B, Peterson MR, Freeman RD. Oblique effect: a neural basis in the visual cortex. *J Neurophysiol* 90: 204-217, 2003.

Livingstone MS, Conway BR. Substructure of direction-selective receptive fields in macaque V1. *J Neurophysiol* 89: 2743-2759, 2003.

Marmarelis PZ, Marmarelis VA. *Analysis of physiological systems.* New York: Plenum, 1978.

Martinez LM, Alonso JM. Construction of complex receptive fields in cat primary visual cortex. *Neuron* 32: 515-525, 2001.

Movshon JA, Lennie P. Pattern-selective adaptation in visual cortical neurones. *Nature*

278: 850-852, 1979.

Movshon JA, Newsome WT. Visual response properties of striate cortical neurons projecting to area MT in macaque monkeys. *J Neurosci* 16: 7733-7741, 1996.

Movshon JA, Thompson ID, Tolhurst DJ. Receptive field organization of complex cells in the cat's striate cortex. *J Physiol* 283: 79-99, 1978a.

Movshon JA, Thompson ID, Tolhurst DJ. Spatial summation in the receptive fields of simple cells in the cat's striate cortex. *J Physiol* 283: 53-77, 1978b.

Nishimoto S, Arai M, Ohzawa I. Accuracy of subspace mapping of spatiotemporal frequency domain visual receptive fields. *J Neurophysiol* 93: 3524-3536, 2005.

Nishimoto S, Ishida T, Ohzawa I. Receptive field properties of neurons in the early visual cortex revealed by local spectral reverse correlation. *J Neurosci* 26: 3269-3280, 2006.

Ohzawa I, DeAngelis GC, Freeman RD. Encoding of binocular disparity by simple cells in the cat's visual cortex. *J Neurophysiol* 75: 1779-1805, 1996.

Ohzawa I, DeAngelis GC, Freeman RD. Stereoscopic depth discrimination in the visual cortex: neurons ideally suited as disparity detectors. *Science* 249: 1037-1041, 1990.

Ohzawa I, Freeman RD. The binocular organization of complex cells in the cat's visual cortex. *J Neurophysiol* 56: 243-259, 1986.

Ohzawa I, Sclar G, Freeman RD. Contrast gain control in the cat visual cortex. *Nature* 298: 266-268, 1982.

Pack CC, Conway BR, Born RT, Livingstone MS. Spatiotemporal structure of nonlinear subunits in macaque visual cortex. *J Neurosci* 26: 893-907, 2006.

Pillow JW, Simoncelli EP. Dimensionality reduction in neural models: an

information-theoretic generalization of spike-triggered average and covariance analysis. *J Vis* 6: 414-428, 2006.

Pollen DA, Gaska JP, Jacobson LD. Physiological constraints on models of visual cortical function. In: *Models of Brain Function*, edited by Cotterill RMJ. Cambridge, UK: Cambridge, 1989.

Prenger R, Wu MC, David SV, Gallant JL. Nonlinear V1 responses to natural scenes revealed by neural network analysis. *Neural Netw* 17: 663-679, 2004.

Reid RC, Alonso JM. Specificity of monosynaptic connections from thalamus to visual cortex. *Nature* 378: 281-284, 1995.

Ringach DL, Bredfeldt CE, Shapley RM, Hawken MJ. Suppression of neural responses to nonoptimal stimuli correlates with tuning selectivity in macaque V1. *J Neurophysiol* 87: 1018-1027, 2002.

Ringach DL, Sapiro G, Shapley R. A subspace reverse-correlation technique for the study of visual neurons. *Vision Res* 37: 2455-2464, 1997.

Rust NC, Schwartz O, Movshon JA, Simoncelli EP. Spatiotemporal elements of macaque v1 receptive fields. *Neuron* 46: 945-956, 2005.

Sanada TM, Ohzawa I. Encoding of three-dimensional surface slant in cat visual areas 17 and 18. *J Neurophysiol* 95: 2768-2786, 2006.

Shapley R, Hochstein S. Visual spatial summation in two classes of geniculate cells. *Nature* 256: 411-413, 1975.

Sharpee T, Rust NC, Bialek W. Analyzing neural responses to natural signals: maximally informative dimensions. *Neural Comput* 16: 223-250, 2004.

Skottun BC, De Valois RL, Grosof DH, Movshon JA, Albrecht DG, Bonds AB. Classifying simple and complex cells on the basis of response modulation. *Vision*

Res 31: 1079-1086, 1991.

Sutter E. A revised conception of visual receptive fields based on pseudorandom spatio-temporal pattern stimuli. *Proceedings of the Conference on Testing and Identification of Nonlinear Systems*, California Institute of Technology, Pasadena, 1975.

Szulborski RG, Palmer LA. The two-dimensional spatial structure of nonlinear subunits in the receptive fields of complex cells. *Vision Res* 30: 249-254, 1990.

Tao L, Shelley M, McLaughlin D, Shapley R. An egalitarian network model for the emergence of simple and complex cells in visual cortex. *Proc Natl Acad Sci U S A* 101: 366-371, 2004.

Touryan J, Lau B, Dan Y. Isolation of relevant visual features from random stimuli for cortical complex cells. *J Neurosci* 22: 10811-10818, 2002.

Toyama K, Kimura M, Tanaka K. Organization of cat visual cortex as investigated by cross-correlation technique. *J Neurophysiol* 46: 202-214, 1981.

Troyer TW, Krukowski AE, Priebe NJ, Miller KD. Contrast-invariant orientation tuning in cat visual cortex: thalamocortical input tuning and correlation-based intracortical connectivity. *J Neurosci* 18: 5908-5927, 1998.

Watson AB, Ahumada AJ, Jr. A look at motion in the frequency domain. *NASA Tech. Memo.* 84352: 1-10, 1983.

Watson AB, Ahumada AJ, Jr. Model of human visual-motion sensing. *J Opt Soc Am A* 2: 322-341, 1985.

A

B

C

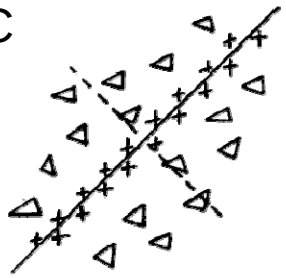

D

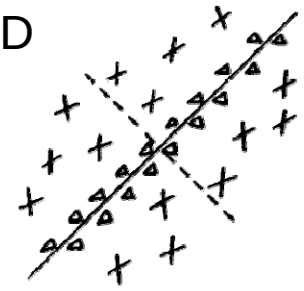

E

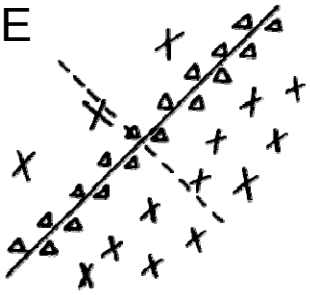

F

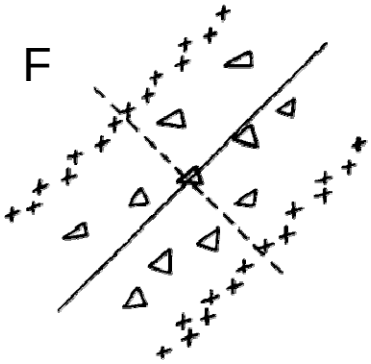

G

Figure 1.1.1. Receptive fields of LGN neurons (***A*** and ***B***) and cortical simple cells in the primary visual cortex (***C***-***G***). Cross symbols indicate areas giving ON responses, while triangle symbols represent areas giving OFF responses. ***A***: ON-center LGN cell. ***B***: OFF-center LGN cell. For cells shown in ***C***-***G***, optimal orientations are shown by continuous lines through receptive field centers. Note that optimal orientations are oblique for all simple cells in the figure, although each arrangement of subregions were observed in all orientations. After Hubel and Wiesel (1962).

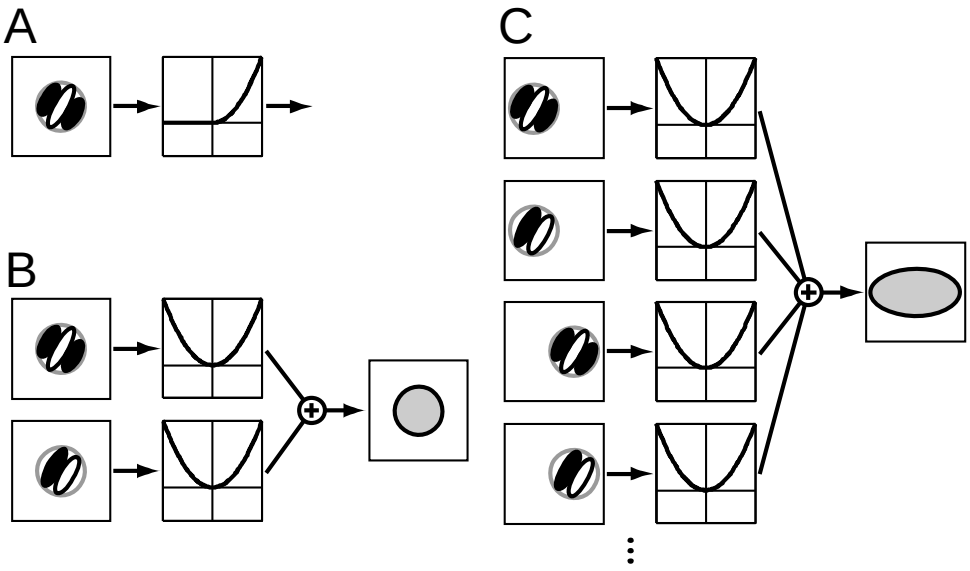
A
B
C

Figure 1.5.1. Schematic illustration of functional models for early visual cortical neurons. ***A*** shows a functional model for simple cells. The response of a simple cell is described by a linear filter whose output is half-wave rectified and squared. ***B*** depicts a minimalist energy model for complex cells, which respond to the visual stimuli of both contrast polarities in the receptive fields. The response invariance to contrast polarity is parsimoniously explained by a quadrature pair (i.e. different in spatial phase by 90°) of linear filters whose outputs are squared and summed. This operation calculates the energy of the preferred spatial frequency components of visual scene in the receptive fields. Since the number of linear filters is minimized in the parsimonious energy model, the receptive field of a complex cell has the same spatial extent as the preceding linear filters. In model ***C***, however, spatial pooling as well as energy computation is an important component to generate the receptive fields of complex cells. In this case, the receptive field of a complex cell is substantially larger than those of the individual linear filters.

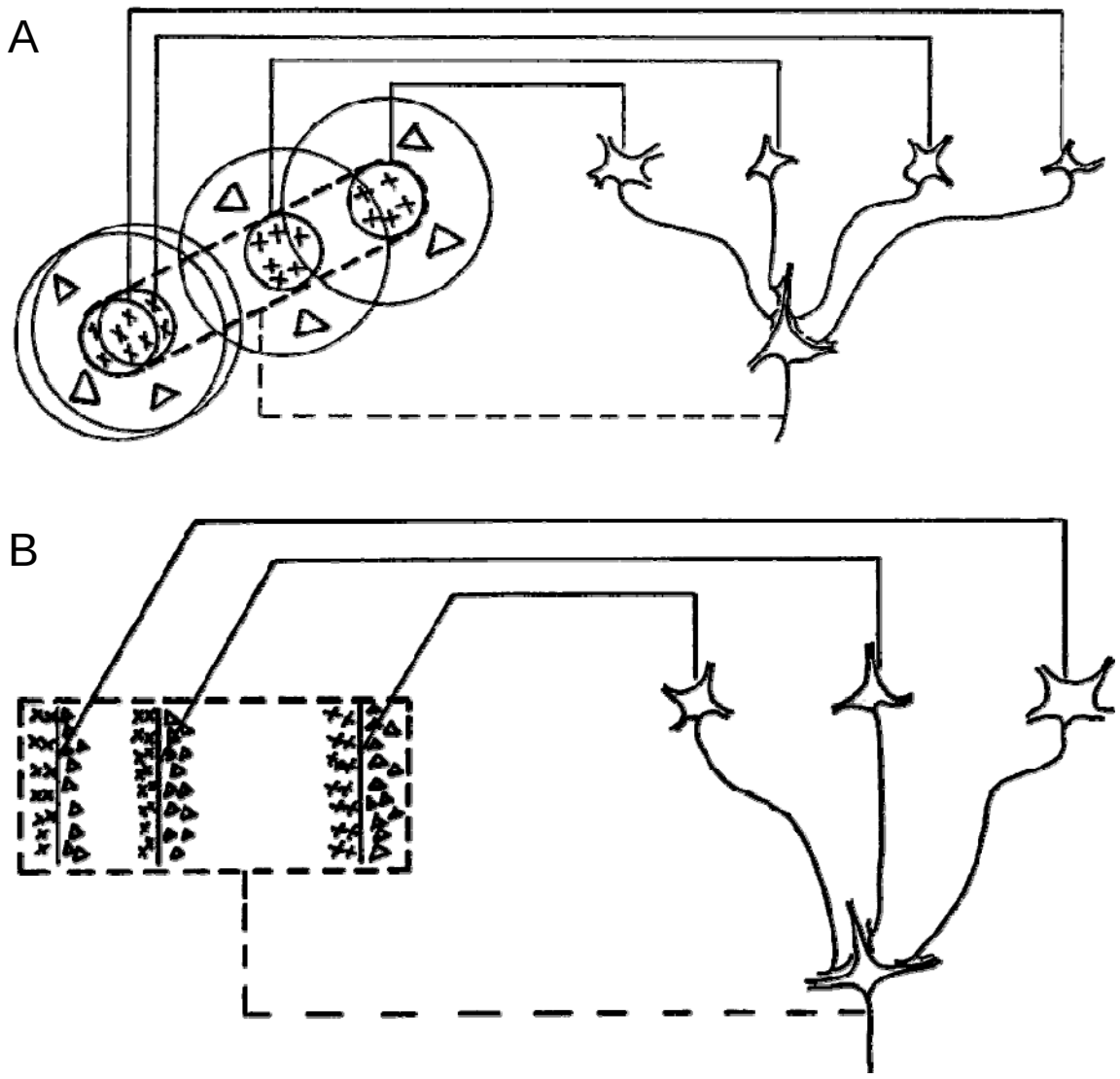
A
B

Figure 1.7.1. Hierarchical models proposed by Hubel and Wiesel (1962). ***A*** and ***B*** illustrates a possible schema for explaining the organization of the receptive fields of simple cells and complex cells, respectively. After Hubel and Wiesel (1962).

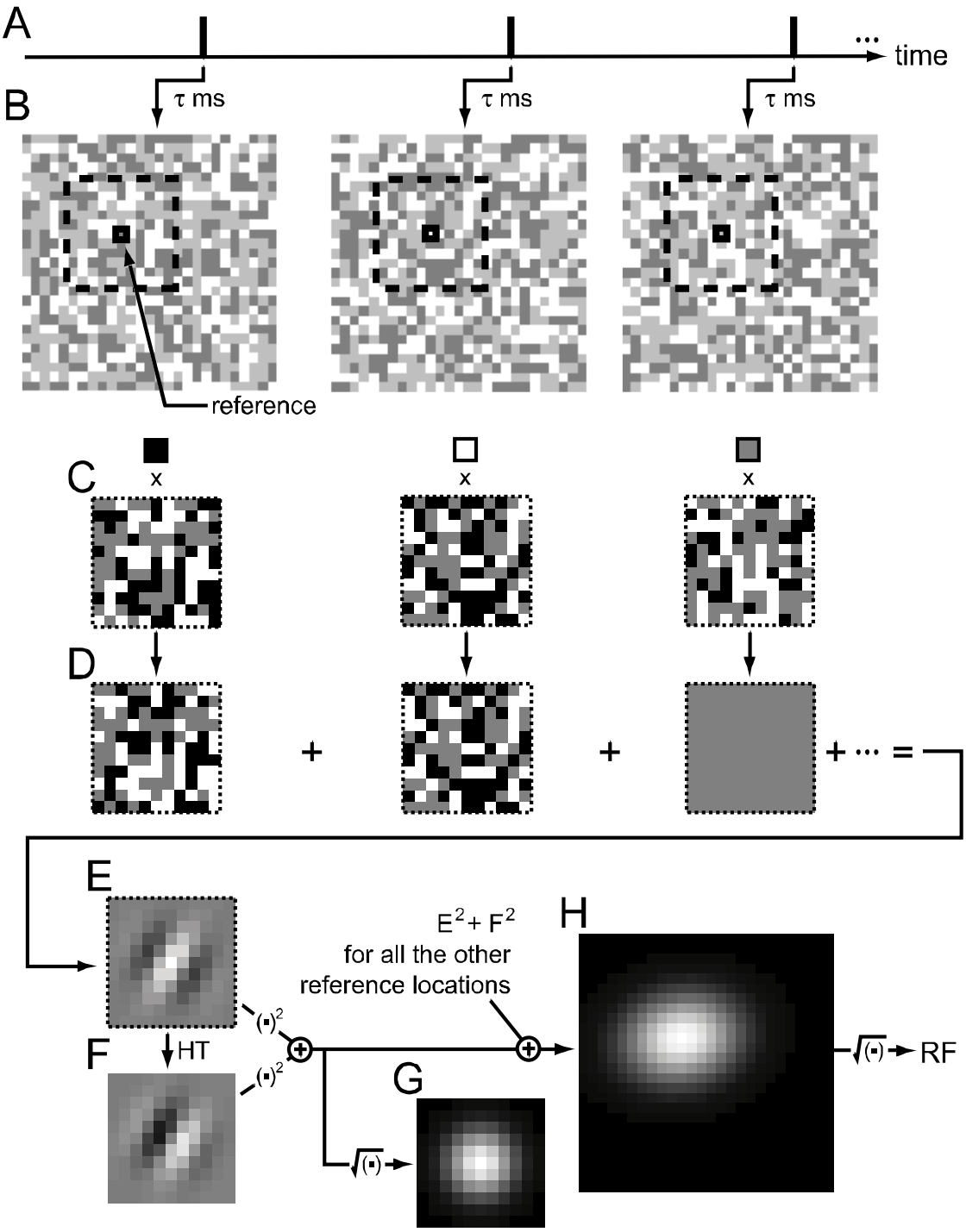
A
time
B
τ ms
τ ms
τ ms
reference
C
x
x
x
D
+
+
+ ··· =
E
F
HT
$(\cdot)^2$
$(\cdot)^2$
$E^2 + F^2$
for all the other
reference locations
G
H
$\sqrt{(\cdot)}$
$\sqrt{(\cdot)}$ RF

Figure 2.5.1. Analysis of second-order interaction to uncover the internal spatial structure of receptive fields for complex cells. ***A***: A spike train was recorded during the presentation of a sequence of two-dimensional dynamic noise stimuli. ***B***: Spike-triggered stimuli were picked up for a particular correlation delay for each spike. ***C, D***: Second-order interaction was analyzed as follows. Reference was fixed at a particular position, and the local stimulus patch was selected for the second-order interaction analysis (***C***). For a dark reference, the contrast of all dots in the patch was reversed (***D***, left). For a bright reference, the contrast of all dots in the patch was retained (***D***, center). In the case of a gray reference, the contrast of all dots in the patch was nullified (***D***, right). These operations correspond to multiplication by –1, 1, and 0 for dark, bright, and gray reference stimuli, respectively. ***E***: A second-order interaction map for the reference location was obtained by accumulating all spike-triggered local stimulus patches that were modified on the basis of the contrast polarity of reference stimuli. The second-order interaction at the reference location cannot be measured, but is required for subsequent analyses such as Fourier transform. Thus, interaction strength at the reference location was interpolated from neighboring values (spline interpolation). ***F***: Partial Hilbert transform (HT) of ***E*** was obtained via Fourier analysis. ***G***: The envelope of the second-order interaction map was computed as the root-mean-square sum of ***E*** and ***F***. Second-order interaction maps and their envelopes were obtained for all reference locations in visual stimuli. ***H***: The overall receptive field of the complex cell was obtained by taking sum of E^2+F^2 of all reference locations and then computing its square root. $(.)^2$ denotes a squaring operation for each matrix element. $(.)^{1/2}$ indicates taking square root for each matrix element.

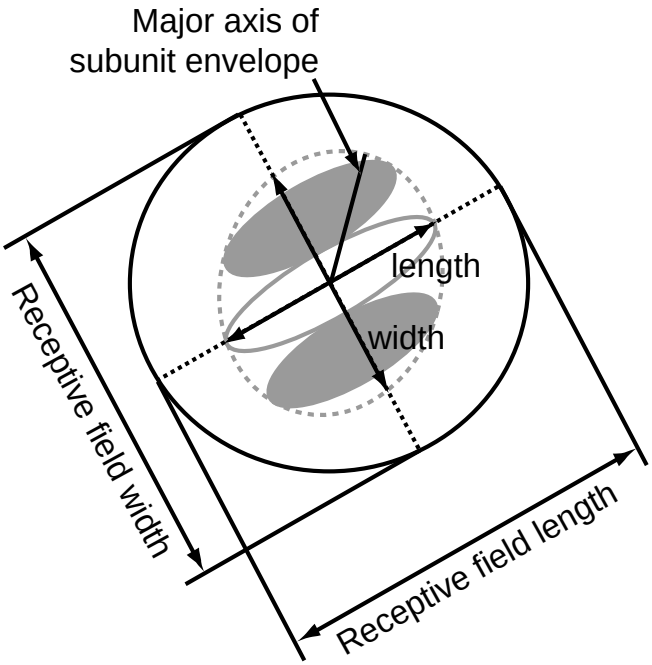
Major axis of
subunit envelope
length
width
Receptive field width
Receptive field length

Figure 2.7.1. Definition of length and width for the subunits and receptive fields of complex cells. First, the bounds of second-order interaction map envelopes (gray dashed ellipse enclosing subregions) and receptive fields (black solid ellipse) were defined by the level that was 5% of the peak of the two-dimensional Gaussian function fitted to them. Then, the length and the width were evaluated for the elliptic region along the parallel and orthogonal axes to the optimal orientation, respectively. Note that the length and the width are independent of the axis of the elliptic elongation for subunit envelopes and receptive fields.

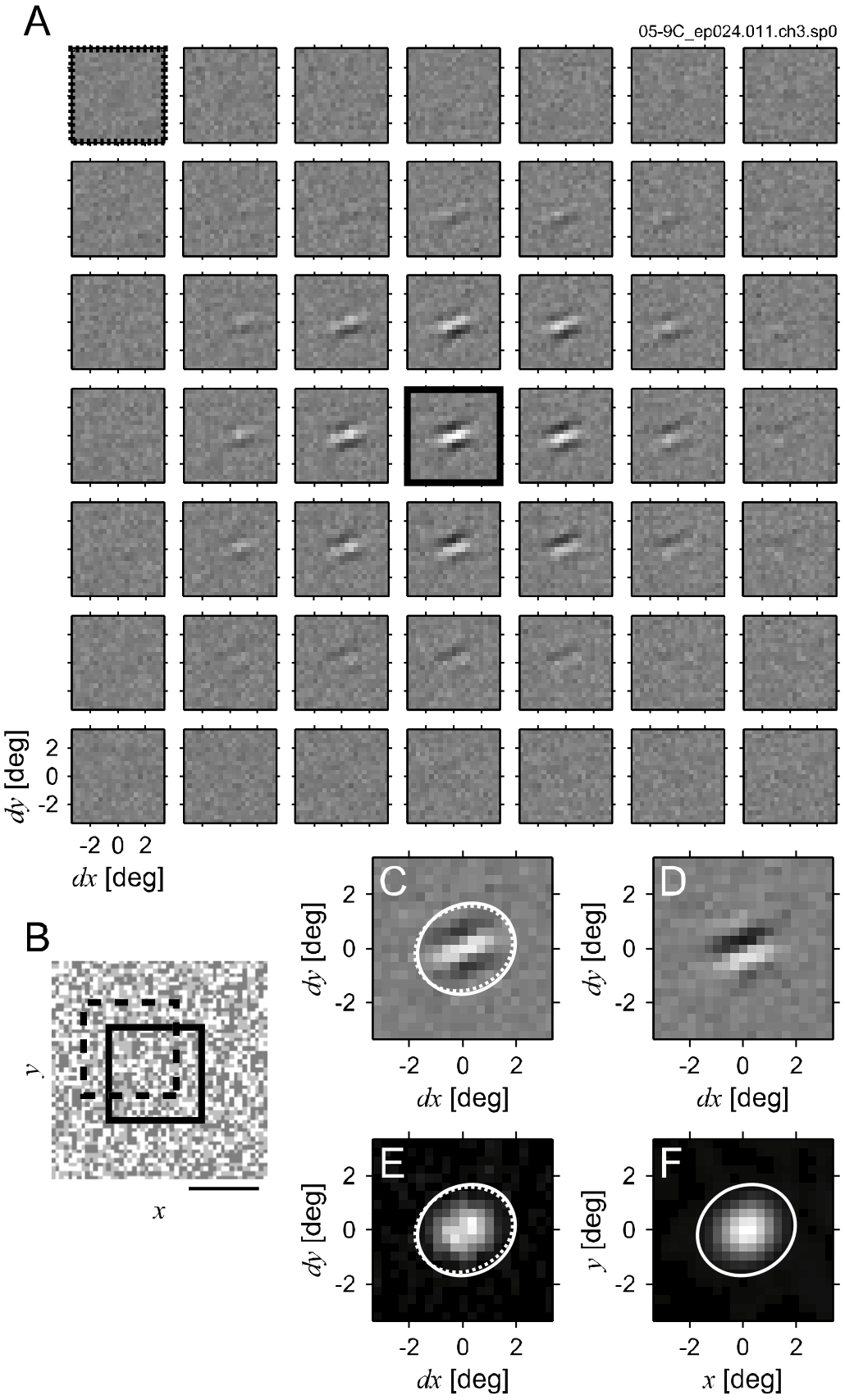
A
05-9C_ep024.011.ch3.sp0
dy [deg]
2
0
-2
-2 0 2
dx [deg]
B
y
x
C
D
E
F
dy [deg]
dx [deg]
y [deg]
x [deg]

Figure 3.1.1. A representative example is shown of the second-order interaction analysis for a complex cell. A second-order interaction map indicates contributions to responses of a second-dot placed near the reference stimulus. This may be calculated from responses to dynamic dense noise stimuli (see *Materials and Methods* for details). ***A*** shows a matrix of second-order interaction maps obtained by selecting a reference position within the stimulated area at two-dot intervals, and arranged according to the relative order of reference positions. Each map consists of 21 × 21 pixels, and the position of the reference stimulus is at the center. Bright pixels represent excitatory responses to stimuli with the same contrast polarity as stimulus at reference (bright-bright or dark-dark), and dark pixels indicate excitatory responses to stimuli with the opposite contrast polarity to stimulus at reference (bright-dark or dark-bright). The interaction map in the center of ***A***, outlined by a solid frame, had the strongest interactions among the maps for all reference locations. This interaction map covered a portion of the stimulus area shown by the solid square in ***B***. (The contrast of noise stimuli in this illustration is reduced for clarity.) The position of the top-left interaction map in ***A*** is also shown by the dashed square in ***B***. A scale bar in ***B*** corresponds to 5°. ***C*** illustrates the bounds of interactions (dashed white ellipse) for the central interaction map in ***A*** (solid frame). Solid white ellipse indicates the bounds of the complex cell receptive field determined from ***F***. ***D*** represents the partial Hilbert transform of the interaction map shown in ***C***. ***C*** and ***D*** form a quadrature pair, and were used to obtain the envelope of the interaction map. ***E*** shows the envelope of the interaction map shown in ***C***. ***F*** shows the overall receptive field for the complex cell. Although the map in ***F*** is defined over the area covered by the dynamic noise stimuli, it is truncated to the same spatial extent as that of ***C***, ***D***, and ***E*** for ease of comparison. The center of the receptive

field is defined as the origin in ***F***, and also corresponds to the origin in ***C***, ***D***, and ***E***. The correlation delay was 53 ms. The optimal spatial frequency, orientation, and areal pooling ratio were 0.25 cycles/degree, 72° and 1.08, respectively.

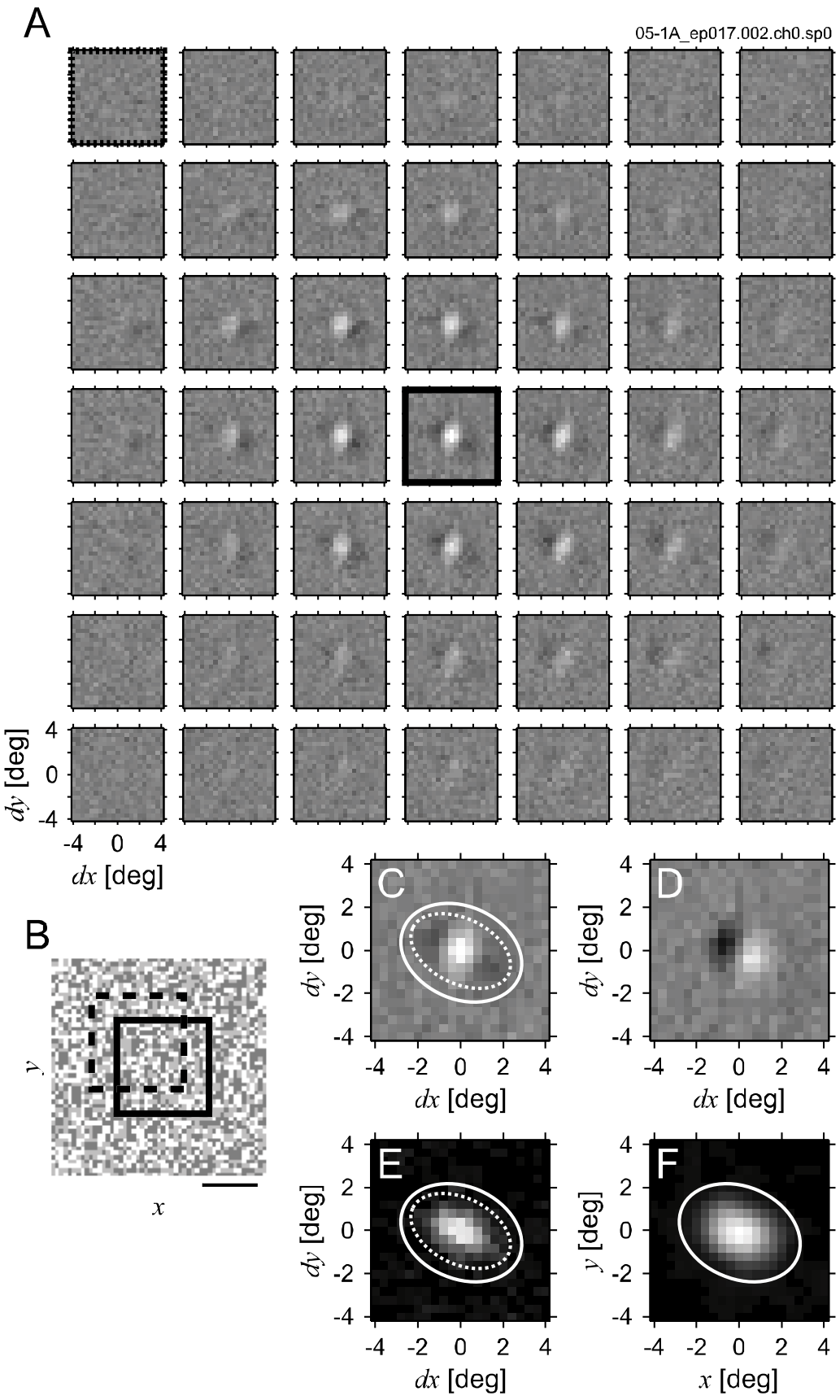
A
05-1A_ep017.002.ch0.sp0
dy [deg]
dx [deg]
B
y
x
C
D
E
F
dy [deg]
dx [deg]
y [deg]
x [deg]

Figure 3.1.2. Another example of the second-order interaction analysis. The format is identical to that of Fig. 3.1.1. See the legend of Fig. 3.1.1. For this complex cell, the strongest second-order interaction was observed at a correlation delay of 39 ms. The optimal spatial frequency and orientation were 0.53 cycles/degree and 22°, respectively. The areal pooling ratio was 1.69, which was significantly larger than one ($P < 0.05$, resampling).

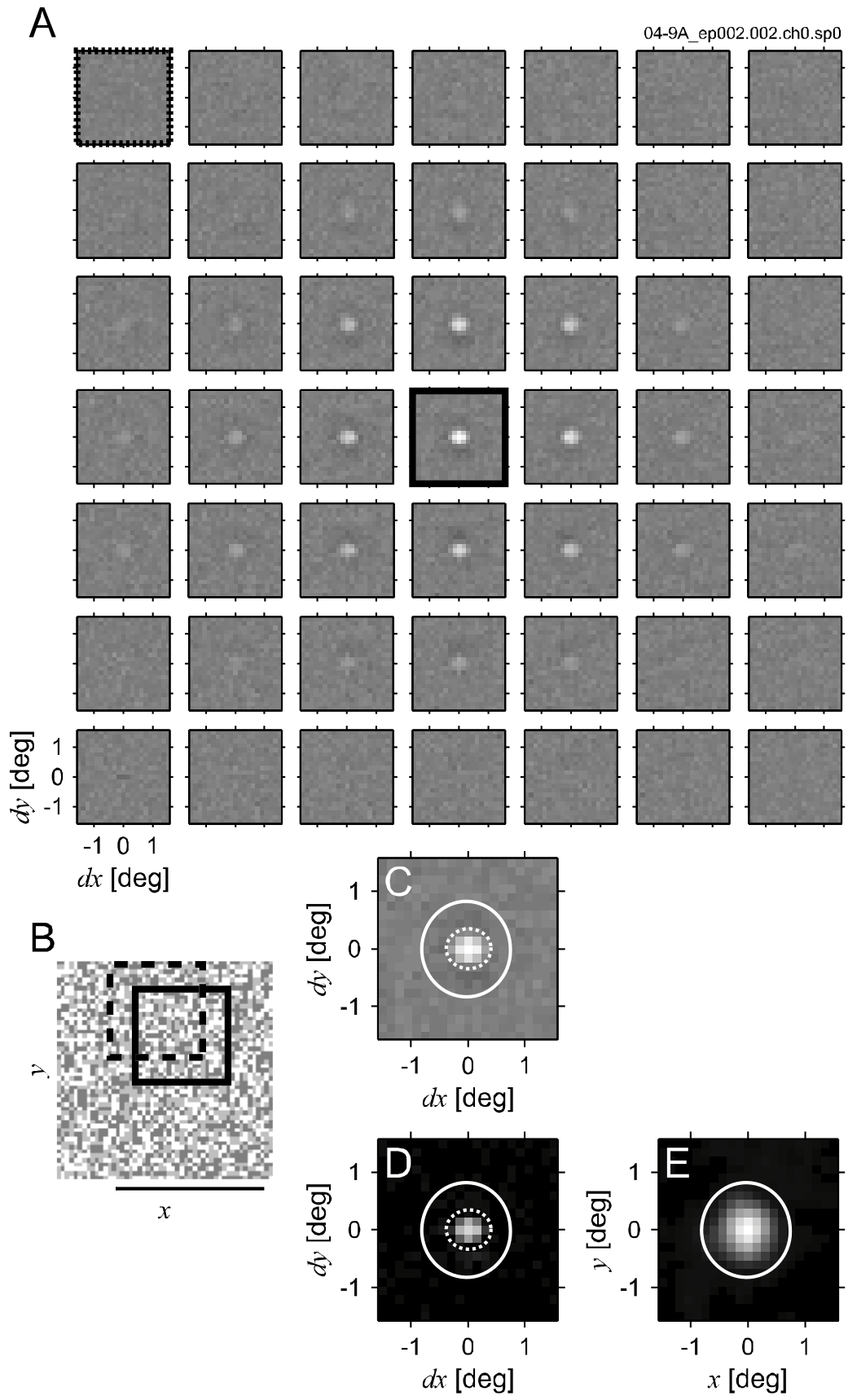
A
04-9A_ep002.002.ch0.sp0
dy [deg]
1
0
-1
-1 0 1
dx [deg]
B
y
x
C
dy [deg]
dx [deg]
D
dy [deg]
dx [deg]
E
y [deg]
x [deg]

Figure 3.1.3. Another example of the second-order interaction analysis. The format is basically the same as that of Fig. 3.1.1. See the legend of Fig. 3.1.1. However, the quadrature counterpart of the interaction map shown in ***C*** is omitted for this example cell, because the orientation tuning of the subunit is not sufficiently strong to define the axis of the partial Hilbert transform. ***D*** shows the envelope of the interaction map shown in ***C***, and ***E*** shows the overall receptive field. The strongest second-order interaction was observed at a correlation delay of 39 ms. The optimal spatial frequency and orientation were 0.86 cycles/degree and 14°, respectively. The areal pooling ratio was 4.73, which was significantly larger than one ($P < 0.05$, resampling).

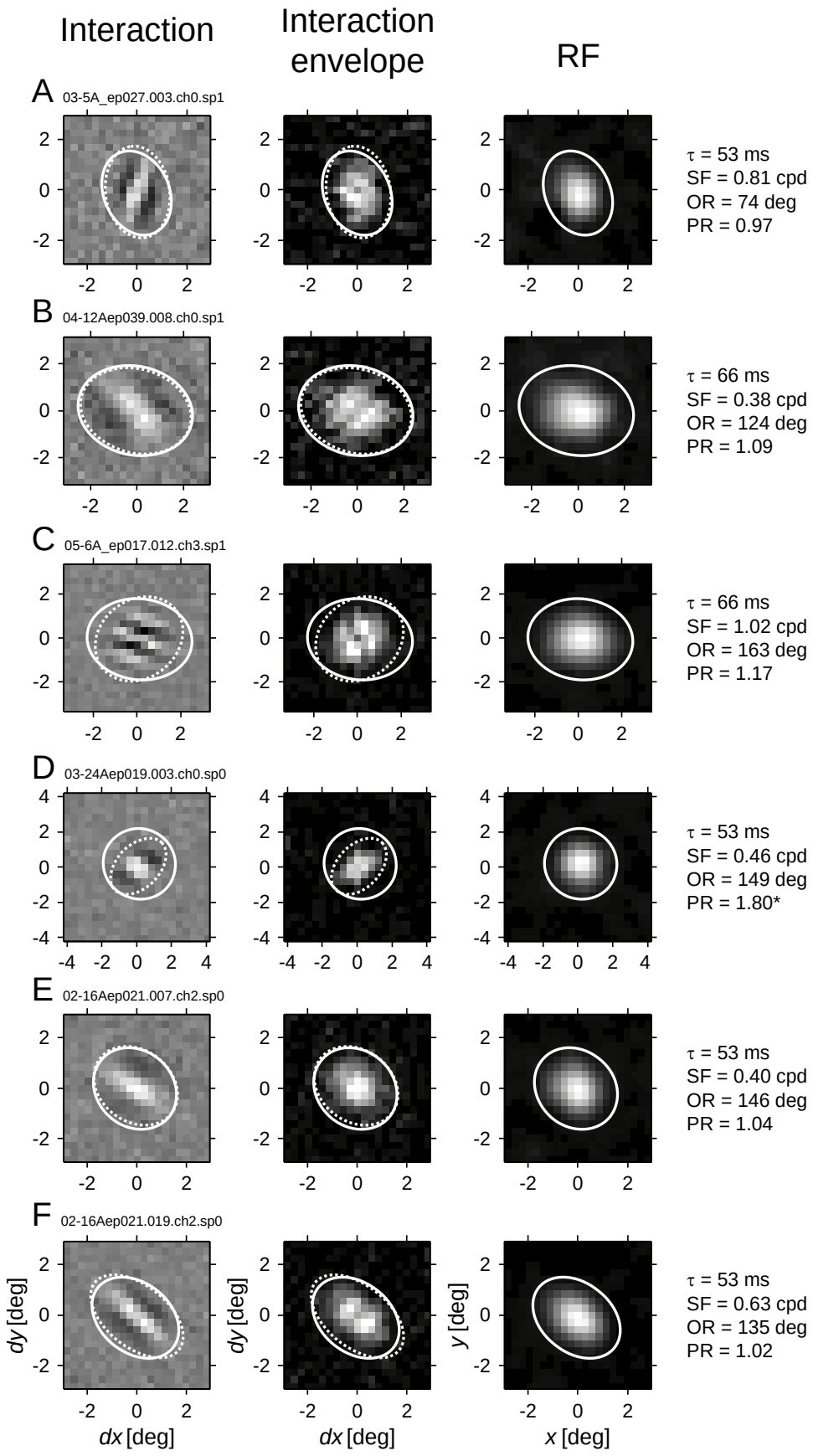
Interaction
Interaction envelope
RF
A
03-5A_ep027.003.ch0.sp1
τ = 53 ms
SF = 0.81 cpd
OR = 74 deg
PR = 0.97
B
04-12Aep039.008.ch0.sp1
τ = 66 ms
SF = 0.38 cpd
OR = 124 deg
PR = 1.09
C
05-6A_ep017.012.ch3.sp1
τ = 66 ms
SF = 1.02 cpd
OR = 163 deg
PR = 1.17
D
03-24Aep019.003.ch0.sp0
τ = 53 ms
SF = 0.46 cpd
OR = 149 deg
PR = 1.80*
E
02-16Aep021.007.ch2.sp0
τ = 53 ms
SF = 0.40 cpd
OR = 146 deg
PR = 1.04
F
02-16Aep021.019.ch2.sp0
τ = 53 ms
SF = 0.63 cpd
OR = 135 deg
PR = 1.02
dy [deg]
dx [deg]
y [deg]
x [deg]

Figure 3.1.4. Examples of the second-order interaction analysis for five additional complex cells. For each analysis, the left panel shows the second-order interaction map that exhibited the strongest interactions, the center panel shows its envelope, and the right panel shows the envelope of the receptive field. Dashed ellipse represents the bounds of the interactions, and solid ellipse delineates those of the receptive field. The origin of the receptive field map corresponds to its center. The optimal correlation delay, spatial frequency (SF), orientation (OR), and areal pooling ratio (PR; $*P < 0.05$, different from one, resampling) are shown to the right of the receptive field for each analysis. ***E*** and ***F*** show the responses of a single complex cell measured for the right and left eye, respectively.

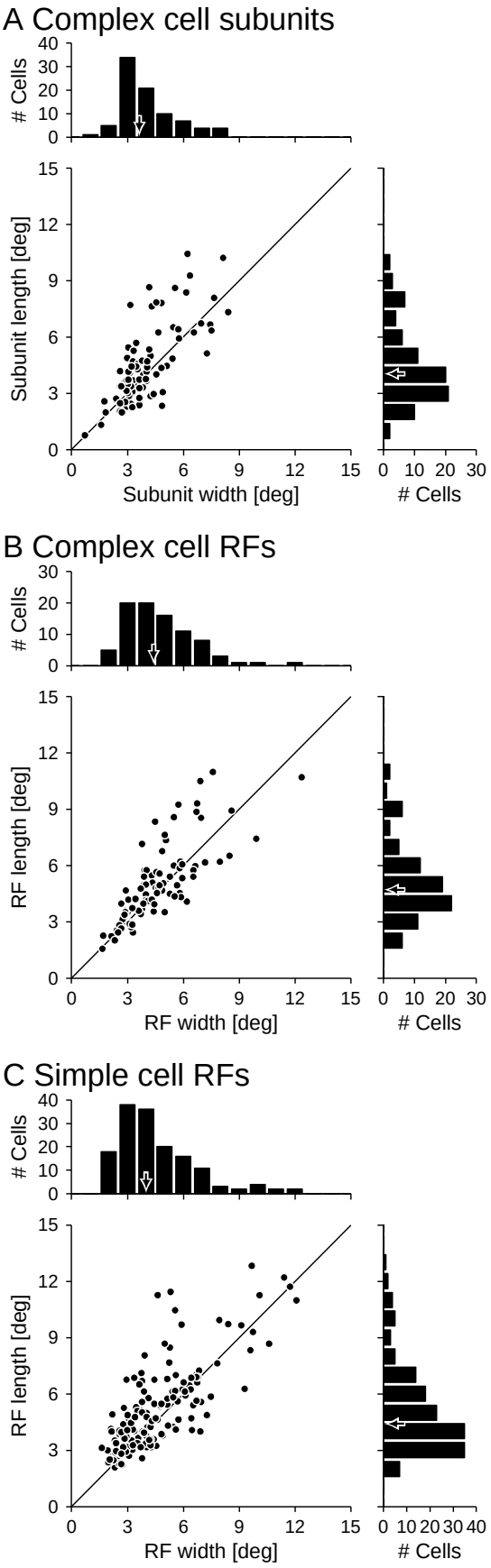
A Complex cell subunits
Cells
Subunit length [deg]
Subunit width [deg]
Cells
B Complex cell RFs
Cells
RF length [deg]
RF width [deg]
Cells
C Simple cell RFs
Cells
RF length [deg]
RF width [deg]
Cells

Figure 3.2.1. Relationships between length and width. ***A***: complex cell subunits. ***B*:** complex cell receptive fields. ***C***: simple cell receptive fields. In the scatter plots, the width is plotted along the horizontal axis, and the length is plotted along the vertical axis. The diagonal line of unity slope indicates a perfect correspondence between the two values. The histograms depict the distributions of the length (right) and the width (upper). Arrows in the histograms indicate the median values for each distribution.

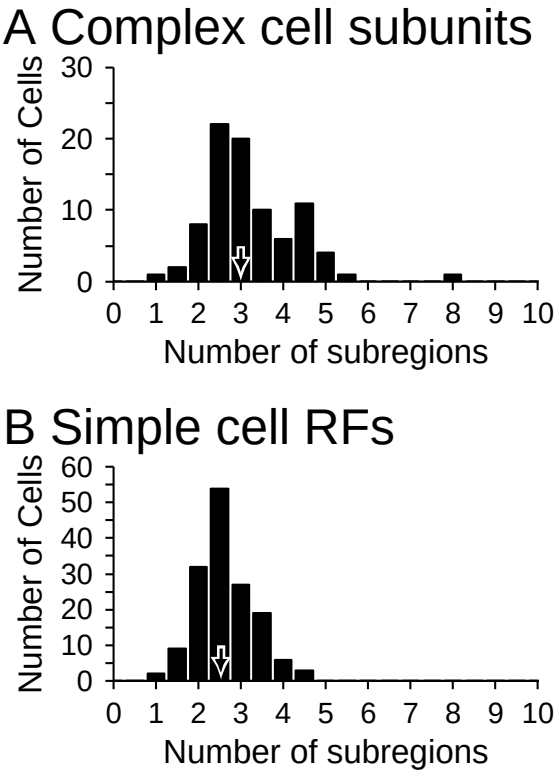
A Complex cell subunits
Number of Cells
30
20
10
0
0 1 2 3 4 5 6 7 8 9 10
Number of subregions
B Simple cell RFs
Number of Cells
60
50
40
30
20
10
0
0 1 2 3 4 5 6 7 8 9 10
Number of subregions

Figure 3.3.1. Distribution of number of subregions. ***A***: within complex cell subunits. ***B***: within simple cell receptive fields. The number of subregions was computed from the width and optimal spatial frequency parameters as described in the section *Number of subregions*. Arrows indicates the medians of each distribution.

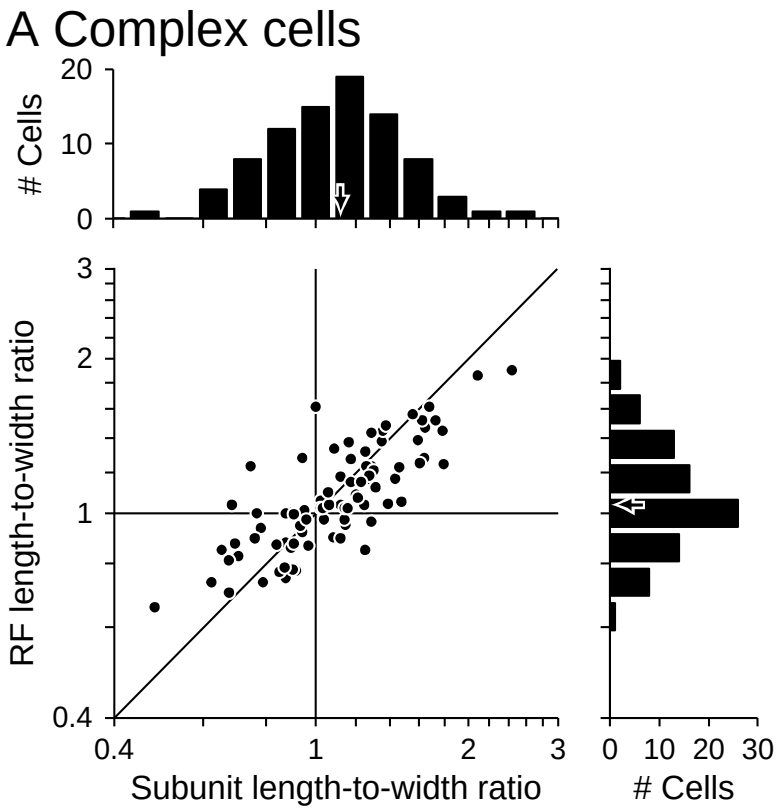
A Complex cells
20
10
0
Cells
3
2
1
0.4
RF length-to-width ratio
0.4
1
2
3
Subunit length-to-width ratio
0
10
20
30
Cells

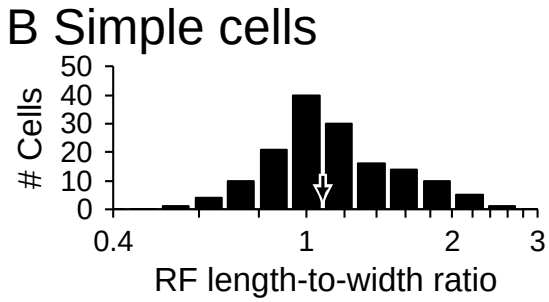
B Simple cells
50
40
30
20
10
0
Cells
0.4
1
2
3
RF length-to-width ratio

Figure 3.4.1. Comparison of length-to-width ratios. ***A*** shows a comparison of the length-to-width ratios on a log-log axis between the subunits and the receptive fields of complex cells. The length-to-width ratios of subunits are plotted along the horizontal axis, and the length-to-width ratios of receptive fields are plotted along the vertical axis. The histograms depict the distributions of the length-to-width ratios of subunits (upper) and receptive fields (right). ***B*** shows the distribution of the length-to-with ratios for simple cell receptive fields. Arrows in the histograms indicate the medians for each distribution.

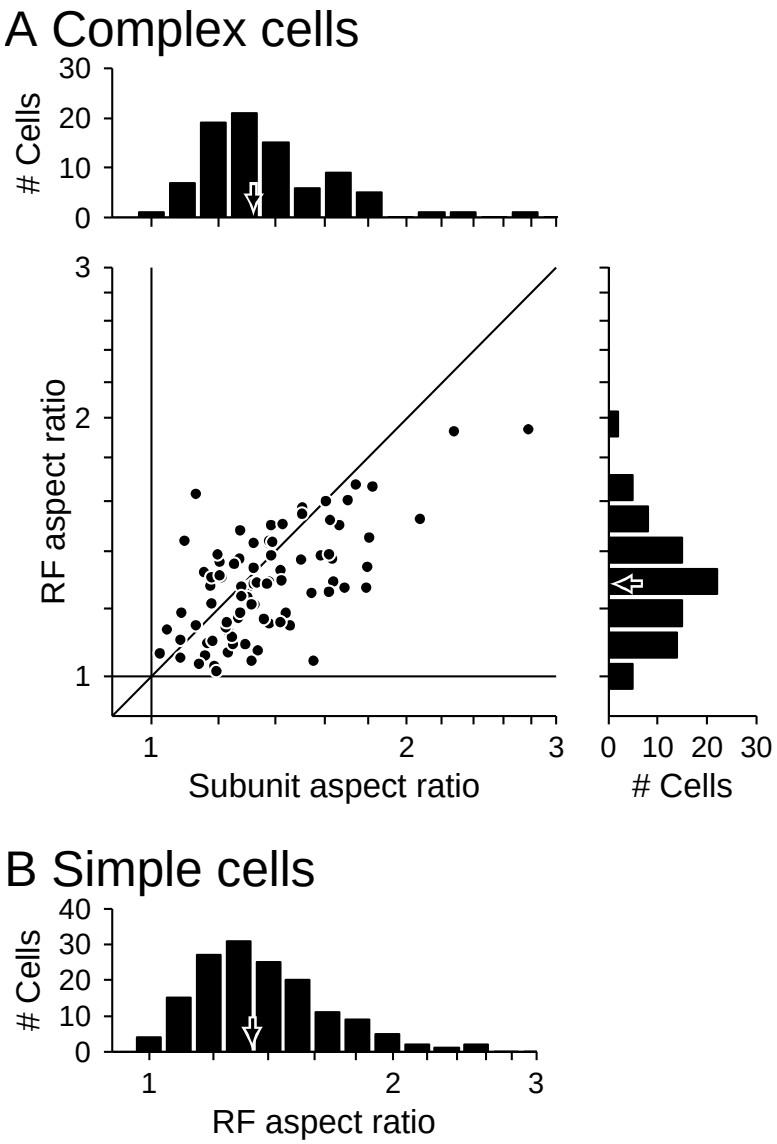
A Complex cells
Cells
30
20
10
0
RF aspect ratio
3
2
1
1
2
3
Subunit aspect ratio
0 10 20 30
Cells
B Simple cells
Cells
40
30
20
10
0
1
2
3
RF aspect ratio

Figure 3.4.2. Comparison of aspect ratios. ***A*** compares the aspect ratios between the subunit envelopes and the receptive fields. The aspect ratios for the subunit envelopes are plotted along the horizontal axis, and those for the receptive fields are plotted along the vertical axis. The comparison is depicted on a log-log coordinate. The histograms illustrate the distributions of the aspect ratios for the subunit envelopes (upper) and the receptive fields (right). ***B*** shows the distribution of the aspect ratios for the receptive field envelopes of simple cells. Arrows in the histograms indicate the medians for each distribution.

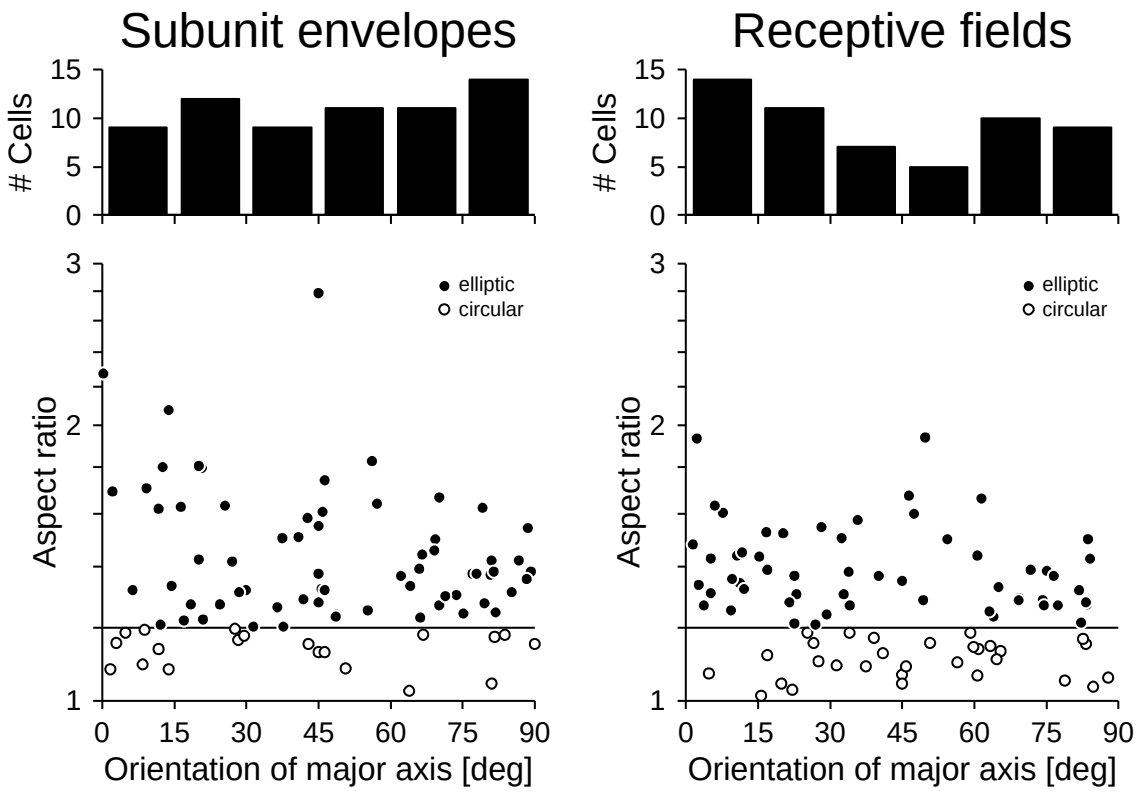
Subunit envelopes
Receptive fields
Cells
15
10
5
0
Aspect ratio
3
2
1
elliptic
circular
0
15
30
45
60
75
90
Orientation of major axis [deg]

Figure 3.5.1. Analysis of anisotropic elongation for the subunit envelopes and the receptive fields of complex cells. The orientation of elongation was measured from the absolute horizontal axis, and clockwise and counter-clockwise rotation was not discriminated. The left panel shows the results of analysis for the subunit envelopes, and the right panel shows those for the receptive fields of complex cells. In the scatter plots, the aspect ratios are plotted against the orientation of the major axis. Filled symbols denote data from cells for which subunit envelopes and receptive fields were sufficiently elliptic (aspect ratio > 1.2; $n = 59$ for subunit envelopes in the left panel; $n = 46$ for receptive fields in the right panel). Open symbols are used for complex cells with nearly circular (aspect ratio ≤ 1.2) subunit envelopes ($n = 27$) and receptive fields ($n = 40$). The histograms depict the distributions of the orientation of the major axis for complex cells with sufficiently elliptic subunit envelopes and receptive fields. The criterion ratio is denoted by a solid horizontal line in the scatter plots.

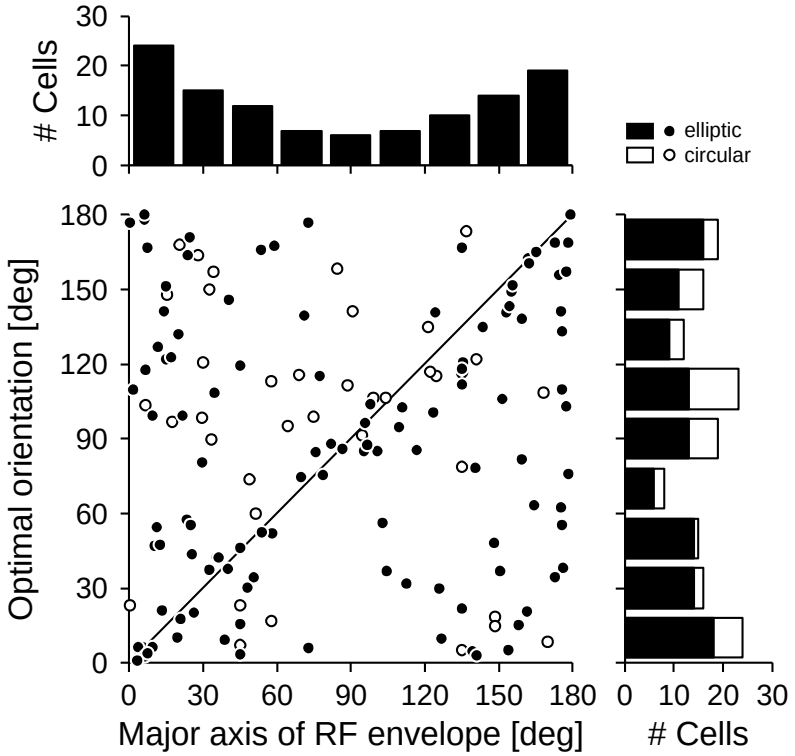
30
20
10
0
Cells
elliptic
circular
180
150
120
90
60
30
0
Optimal orientation [deg]
0
30
60
90
120
150
180
Major axis of RF envelope [deg]
0
10
20
30
Cells

Figure 3.5.2. Analysis is shown of a possible relationship between the axis of receptive field elongation and the optimal orientation for simple cells. The scatter plot compares the optimal orientation and the orientation of the major axis of receptive field envelopes for simple cells. Angle was gauged counterclockwise from the horizontal axis (horizontal orientation and elongation correspond to 0°, whereas vertical correspond to 90°). In the scatter plot, filled symbols denote data from cells for which receptive field envelopes were sufficiently elliptic (aspect ratio > 1.2; n = 114), and open symbols represent data from neurons of which receptive field envelopes were not elongated, i.e., nearly circular (aspect ratio ≤ 1.2; n = 38). The histograms depict the distributions of optimal orientation (right) and the orientation of the major axis for the receptive field envelopes (top). Only cells with sufficiently elliptic receptive field envelopes were counted for the histogram at top.

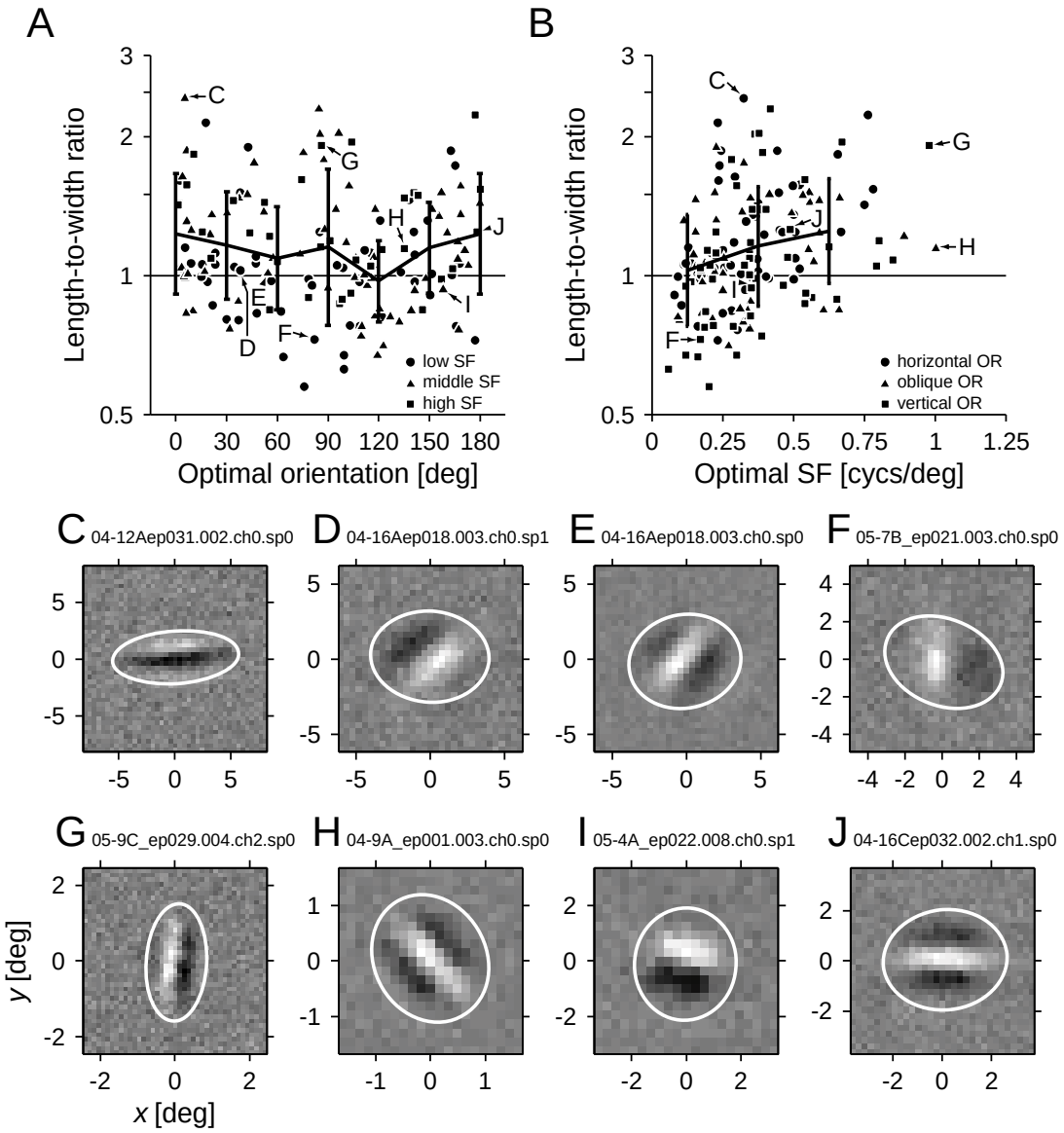
A
B
Length-to-width ratio
Optimal orientation [deg]
Optimal SF [cycs/deg]
low SF
middle SF
high SF
horizontal OR
oblique OR
vertical OR
C 04-12Aep031.002.ch0.sp0
D 04-16Aep018.003.ch0.sp1
E 04-16Aep018.003.ch0.sp0
F 05-7B_ep021.003.ch0.sp0
G 05-9C_ep029.004.ch2.sp0
H 04-9A_ep001.003.ch0.sp0
I 05-4A_ep022.008.ch0.sp1
J 04-16Cep032.002.ch1.sp0
y [deg]
x [deg]

Figure 3.5.3. Relationship with the length-to-width ratio is examined for the optimal orientation and spatial frequency for simple cells. ***A*** depicts the length-to-width ratio against the optimal orientation as a scatter plot. Circles, triangles, and square symbols indicate neurons which prefer low (< 0.25 cpd), middle (≥ 0.25 cpd and < 0.5 cpd), and high (≥ 0.5 cpd) spatial frequencies, respectively. The cut-off values are arbitrary. The mean length-to-width ratios were calculated for each group of cells categorized based on the optimal orientation, and were superimposed in the scatter plot by a solid curve. Error bars indicate the SDs. The receptive fields of cells pointed to by arrows (***C***-***J***) are shown in the bottom corresponding panels. ***B*** plots the length-to-width ratio against the optimal spatial frequency. Circles, triangles, and square symbols represent neurons tuned to horizontal (within 30° of horizontal), oblique, and vertical (within 30° of vertical), respectively. A solid curve and bars indicate the mean ± SD values of the length-to-width ratios for each population of neurons grouped on the basis of the optimal spatial frequency. The cut-off values are the same as in ***A***. The neurons labeled in ***A*** are also indicated by arrows in ***B*** except for cells ***D*** and ***E***, which are located in the dense cluster of symbols near (0.2, 1). ***C***-***J*** illustrate the receptive fields of simple cells which are indicated by arrows in ***A*** and ***B***. Bright regions indicate ON subregions, whereas dark regions denote OFF subregions. Solid ellipses indicate the extents of receptive fields determined as 5% of the peak of the fitted Gaussian envelopes. The center of each receptive field is defined as the origin. The optimal correlation delay, spatial frequency (SF), orientation (OR), and length-to-width ratio (LWR) for ***C***-***J*** were as follows, respectively: τ = 55, 42, 43, 54, 52, 51, 46, and 49 ms; SF = 0.32, 0.17, 0.25, 0.17, 0.98, 1.00, 0.33, and 0.50 cycles/deg; OR = 5°, 38°, 54°, 82°, 86°, 135°, 158° and 178°; LWR = 2.43, 1.03, 1.01, 0.73, 1.92, 1.15, 0.93, and 1.24.

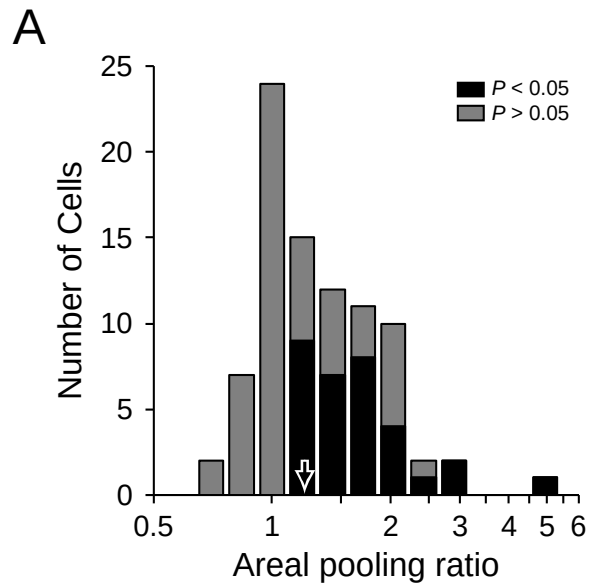
A
25
20
15
10
5
0
Number of Cells
P < 0.05
P > 0.05
0.5
1
2
3
4
5
6
Areal pooling ratio

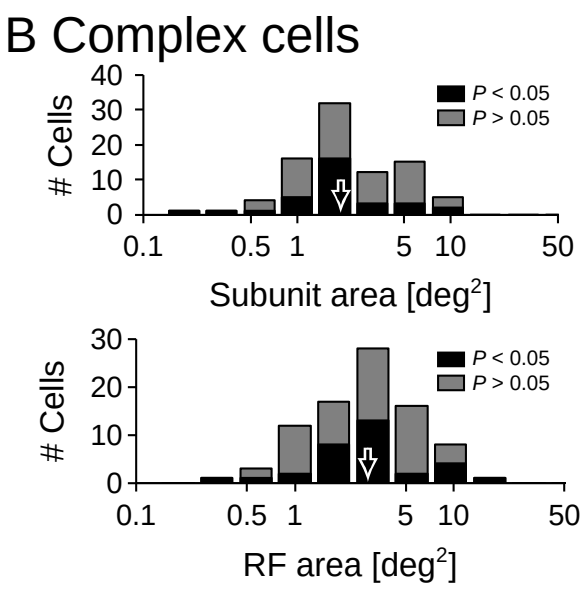
B Complex cells
40
30
20
10
0
Cells
P < 0.05
P > 0.05
0.1
0.5
1
5
10
50
Subunit area [deg2]
30
20
10
0
Cells
P < 0.05
P > 0.05
0.1
0.5
1
5
10
50
RF area [deg2]

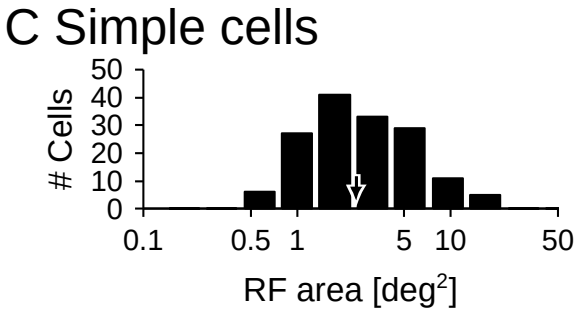
C Simple cells
50
40
30
20
10
0
Cells
0.1
0.5
1
5
10
50
RF area [deg2]

Figure 3.6.1. Analysis of spatial pooling for subunits in complex cells and the receptive field size of simple cells. ***A*** shows the distribution of pooling ratios used to evaluate the degree of the spatial pooling of subunits. An areal pooling ratio was defined as the receptive field area divided by the subunit envelope area. Black bars highlight neurons for which the areal pooling ratios exhibit statistically significant deviation from one ($P < 0.05$, resampling). The minimalist energy model for complex cells predicts the areal pooling ratios close to one. The median of the distribution is indicated by an arrow. ***B*** shows the distributions of the areas of complex cell subunits (upper) and receptive fields (lower). Black and gray bars indicate complex cells with and without significant spatial pooling, respectively (P value = 0.05, resampling). ***C*** depicts the distribution of the areas of simple cell receptive fields. Arrows in the histograms indicate the medians for each distribution.

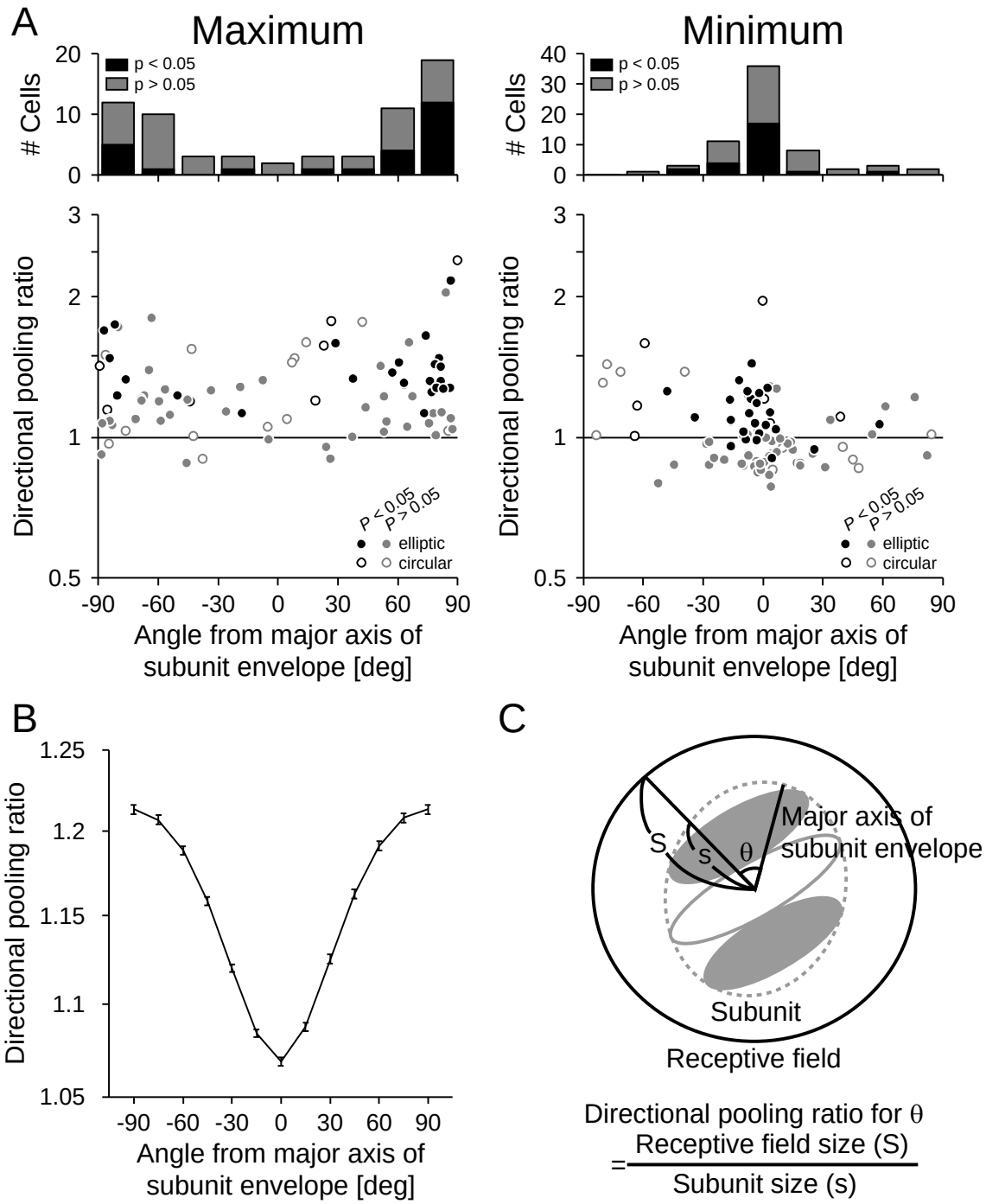
A
Maximum
Minimum
Cells
p < 0.05
p > 0.05
Directional pooling ratio
P < 0.05
P > 0.05
elliptic
circular
Angle from major axis of subunit envelope [deg]
B
Directional pooling ratio
Angle from major axis of subunit envelope [deg]
C
Major axis of subunit envelope
S
s
θ
Subunit
Receptive field
Directional pooling ratio for θ
= Receptive field size (S) / Subunit size (s)

Figure 3.6.2. Analysis of radial anisotropy of spatial pooling for subunits in complex cells. The degree of spatial pooling was evaluated directionally along radial axes that were at various angles with the major axis of the subunit envelope. A directional pooling ratio was defined as the receptive field size divided by the subunit size, measured along a particular radial axis, as schematically illustrated in ***C***. ***A***: The scatter plots show relationships between the maximal (left) or the minimal (right) pooling ratios, and directional angles at which they were obtained. Black symbols represent complex cells for which areal pooling ratios were significantly larger than one ($P < 0.05$, resampling). Gray symbols denote neurons without significant pooling. Filled circles indicate neurons with sufficiently elliptic subunit envelopes, which ensure reliable determination of their major axes (aspect ratio > 1.2). The remaining cells are shown by open symbols. The histograms in ***A*** illustrate the distributions of directional angles to obtain the maximal and the minimal directional pooling ratios. To examine the distributions, complex cells with sufficiently elliptic subunit envelopes were selected. Following the convention used in the scatter plots, black bars indicate neurons with significant spatial pooling, and gray bars represent neurons without significant pooling. ***B*** plots the geometric mean values of directional pooling ratios across neurons against angle from the subunit major axis. Error bars indicate SEs. ***C*** illustrates definition of directional pooling ratio, which was measured at an angle with the major axis of the subunit envelope. By changing the angle parameter, the maximal and minimal size ratios were searched between the subunit and the receptive field.

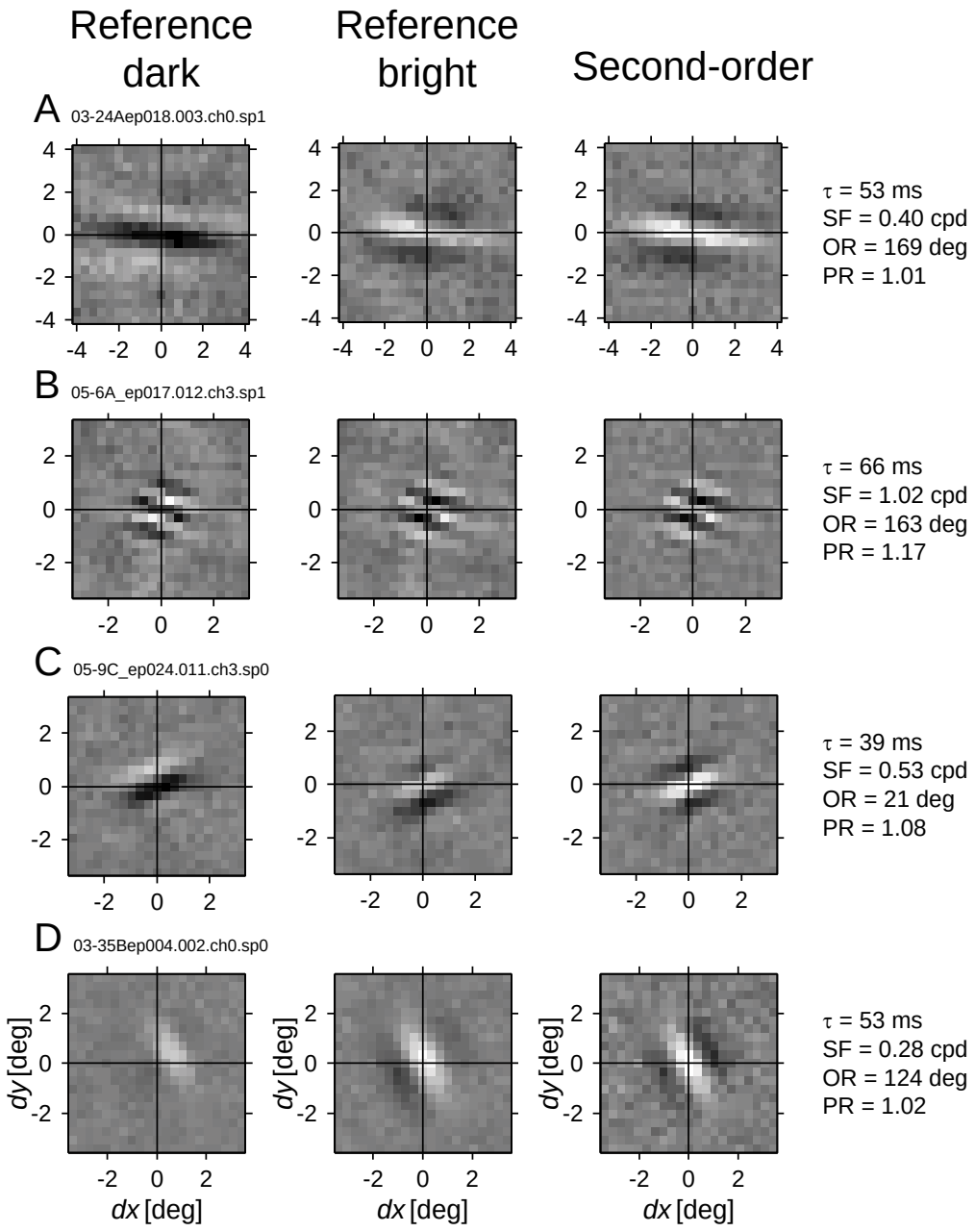
Reference dark
Reference bright
Second-order
A
03-24Aep018.003.ch0.sp1
τ = 53 ms
SF = 0.40 cpd
OR = 169 deg
PR = 1.01
B
05-6A_ep017.012.ch3.sp1
τ = 66 ms
SF = 1.02 cpd
OR = 163 deg
PR = 1.17
C
05-9C_ep024.011.ch3.sp0
τ = 39 ms
SF = 0.53 cpd
OR = 21 deg
PR = 1.08
D
03-35Bep004.002.ch0.sp0
τ = 53 ms
SF = 0.28 cpd
OR = 124 deg
PR = 1.02
dy [deg]
dx [deg]

Figure 3.7.1. Examples of bright-minus-dark maps for four complex cells. The bright-minus-dark maps were calculated separately for dark and bright reference stimuli. For each cell, the left panel shows the map for a dark reference, the center panel shows that for a bright reference, and the right panel shows the second-order interaction map, which is the difference between the center and left maps. These maps were obtained at the same reference location at which the strongest second-order interaction was observed. The reference location is indicated by the cross hairs. The optimal correlation delay, spatial frequency (SF), orientation (OR), and areal pooling ratio (PR) for second-order interaction maps are indicated to the right of the interaction maps for each cell. Cells shown in ***B*** and ***C*** are identical to those in Figs. 3.1.4***C*** and 3.1.2, respectively.

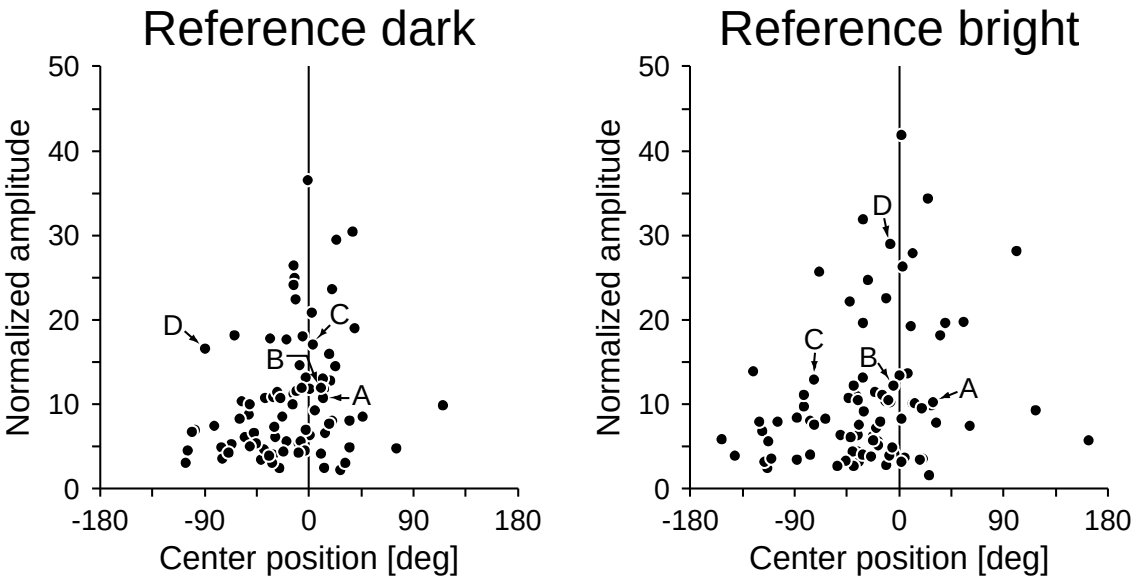
Reference dark
Reference bright
Normalized amplitude
Center position [deg]
50
40
30
20
10
0
-180
-90
0
90
180
A
B
C
D

Figure 3.7.2. Analysis of center position for the envelopes of bright-minus-dark maps for dark (left) and bright (right) reference stimuli. The center position was defined with respect to the reference location, and plotted along the horizontal axis as spatial phase angle for the optimal spatial frequency. The envelope and the center were computed for each two-dimensional map, but only the offset perpendicular to the optimal orientation (obtained by projecting the center onto the width axis) is shown in these figures. The optimal spatial frequency and orientation were extracted via the Fourier analysis from the second-order interaction map. The amplitude was divided by the SD of values on the edges (1-pixel wide) of the bright-minus dark map envelope, and plotted along the vertical axis. The maps for complex cells pointed to by arrows (***A***-***D***) are shown in the corresponding rows in Fig. 3.7.1.

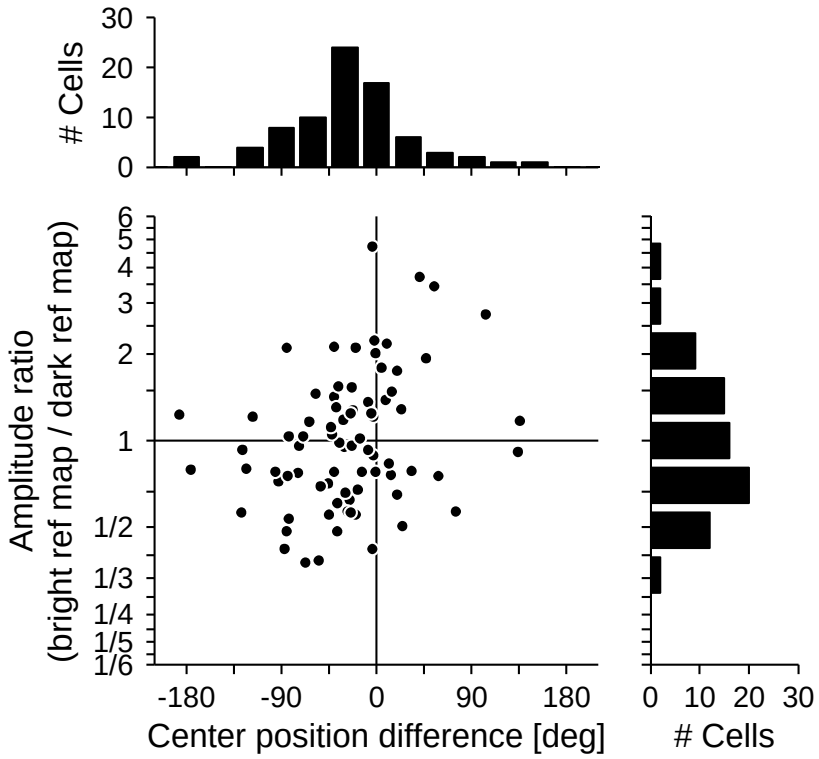
30
20
10
0
Cells
6
5
4
3
2
1
1/2
1/3
1/4
1/5
1/6
Amplitude ratio
(bright ref map / dark ref map)
-180
-90
0
90
180
Center position difference [deg]
0
10
20
30
Cells

Figure 3.7.3. Distributions of center position difference and amplitude ratio between the maps for dark and bright references. The position difference is expressed in terms of a phase angle for the spatial frequency of the subunit. The values were computed relative to the parameters for the dark reference map. Therefore, the amplitude ratios greater than one indicate that the bright-reference maps are stronger than the dark-reference map, while those smaller than one indicate the opposite. For this analysis, only those cells were selected for which normalized amplitudes exceeded three for both dark and bright reference stimuli (n = 78). See also the legend of Fig. 3.7.2.

Table 4.1. Summary of results. The upper part summarizes comparisons between subunits and receptive fields to examine the minimal model for complex cells. The lower part summarizes comparisons between complex cell subunits and simple cell receptive fields to examine whether they are equivalent to each other. The comparison of spatial extents is based on length, width, and areal size, whereas the comparison of spatial shape is based on aspect ratios, length-to-width ratios, and the orientation of elongation. Brief comments and relevant examples are given in the rightmost column.

Comparisons of complex cell receptive fields and their subunits		
Spatial extents	✓	Receptive fields are slightly larger (mean areal ratio = 1.2)
Spatial shape	✓	Receptive fields are slightly more circular than subunits.
Response maps for bright and dark references	×	Response strengths can be imbalanced (e.g. Figs. 3.7.1*C* and *D*). Center positions can be different (e.g. Fig. 3.7.1*D*).

Comparisons of complex cell subunits and simple cell receptive fields		
Spatial extents	✓	Similar
Number of subregions	×	Complex cell subunits have more subregions than simple cells.
Spatial shape	×	Envelopes of simple cell receptive fields tend to be elongated more horizontally than vertically (e.g. Figs. 3.5.3*C*-*F*, and *J*).

Acknowledgements

Many people have contributed to this dissertation, directly or indirectly, knowingly and unwittingly. I would like to take the opportunity to thank them.

I am grateful to my advisor, Izumi Ohzawa, for generously providing the means, encouragement, and freedom to pursue this project. Thanks to Yasushi Kobayashi for always reminding me of biological perspectives. I like Hiroki Tanaka's attitude, which keeps a distance from an easygoing usage of reverse correlation techniques. I thank Makoto Hatanaka, and Aiko Yamori, and Takako Tanaka for maintenance and improvement of our research environment.

I embarked on experiments in this field by using an optical imaging setup with Sakiko Noka. Masashi Iida joined us, and it took two years to succeed in optical imaging based on intrinsic signals. I was fully engaged in electrophysiological experiments eventually. The first serious commitment to electrophysiology involved development of visual neurons and efficient encoding of sensory information: how early postnatal visual experience influences the receptive field structure of individual neurons in the early visual cortex. This work has been collaborated mainly with Taihei Ninomiya. Special thanks to Yuka Tabuchi for her inspiration and perspiration, which now leads me to an information-theoretic approach in an attempt to identify a full set of filters underlying single neurons in the early visual cortex.

Thanks to Rui Kimura for valuable and funny discussions from science to miscellaneous things, which work as morale supports. I thank Masayuki Fukui, Miki Arai, Tsugitaka Ishida, and Yusuke Asada for their help in physiological recording. I cannot help but notice that many guys already left our laboratory to live a new life.

Among them, I especially thank to Akihisa Moriya, Aki Kyouzu, and Naoki Shigaki for friendship, and Shinji Nishimoto and Takahisa Sanada for colleagueship.

Last but not least, thanks to my family for their giving me supports in many ways and letting me do what I wish to do.

Publication list

Original papers

Sasaki KS, Ohzawa I. Internal spatial organization of receptive fields of complex cells in the early visual cortex. *J Neurophysiol* 2007 (in press).

Meeting abstracts

Sasaki K, Ohzawa I. Internal spatial organization of receptive fields of complex cells in the early visual cortex. The society for Neuroscience 36th Annual Meeting, 36: 11.8, Atlanta, USA, Nov., 2006.

Sasaki K, Ohzawa I. Spatial organization of receptive fields of complex cells in the early visual cortex. Neuroscience research, 55 Supplement 1: OS3P-4-07, 2006.

Tabuchi Y, Sasaki K, Ohzawa I. Consistency of simple cell receptive fields: space and spatial frequency domain measurements. Neuroscience research, 55 Supplement 1: PS4A-F099, 2006.

Sasaki K, Ohzawa I. An optimal function for receptive fields of simple cells in the primary visual cortex. The society for Neuroscience 35th Annual Meeting, 35: 618.1, Washington DC, USA, Nov., 2005.